NTNU – Trondheim
Norwegian University of
Science and Technology

Numerical Modelling of Turbulent Boundary Layer

Ida Hystad

Marine Technology (2-year)
Submission date: July 2014
Supervisor: Håvard Holm, IMT
Co-supervisor: Bjørn Anders Pettersson Reif, FFI

Norwegian University of Science and Technology
Department of Marine Technology

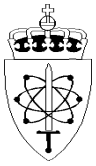

Forsvarets forskningsinstitutt

MASTER THESIS IN MARINE HYDRODYNAMICS

SPRING 2014

for

Stud. techn. Ida Synnøve Hystad

NUMERICAL MODELLING OF TURBULENT BOUNDARY LAYER

Towed acoustic arrays are used in both military and civilian applications. The system consist of thin, very long cables that are submerged in water and towed by a surface ship, a submarine or an unmanned underwater vehicles (UUVs). A relative thick axisymmetric boundary layer is formed along the antenna, but occasionally the cable is rotating rapidly around its axis due to variation in tension caused by e.g. ship movement (tugging).

FFI is currently using advanced CFD methods (LES and DNS) to compute the boundary layer, but it is of interest to investigate simpler methods based on the Reynolds-averaged Navier-Stokes (RANS) approach. The simulations will be conducted using OpenFOAM.

Preface

This report concludes the two year master education in Marine Hydrodynamics at the Department of Marine Technology, NTNU. The problem in question was provided by the Norwegian Defence Research Establishment (FFI). I would like to thank my supervisor at FFI Bjørn Anders Pettersson Reif for his guidance and motivation. I am grateful to Håvard Holm who has provided help and advice. The regular meetings ensured progress in the work with the thesis.

A special thanks to Håkon Strandenes for shearing his knowledge in the use of OpenFOAM. I would also like to thank Mia Prsic and Tufan Arslan for helpful discussions in the field of RANS simulation. The HPC facility as a part of the NOTUR project is also acknowledged.

Trondheim, July 2014

Ida Synnøve Hystad

Abstract

Most physical problems involving viscous fluid flows are characterized by turbulence where instabilities and large velocity gradients generate fluctuations in the flow field. Towed sonar arrays are exposed to turbulence in the boundary layer formed around the cable. Problems are related to the cable rotating around its own axis due to variations in tension force caused by the towing vehicle. Numerical calculations of a pressure driven flow along a cylinder are performed for the purpose of investigating the turbulent boundary layer around the cable. In this study, the numerical software OpenFOAM has been used in order to solve the flow field. The Reynolds Average Navier-Stokes (RANS) approach was applied, providing a time-average solution of the flow quantities. The results were used in a comparative study with data obtained from Large Eddy Simulation (LES).

Simulations were carried out for two Reynolds numbers based on the shear velocity; $Re_\tau = [240,\ 550]$. The cylinder was assigned two different rotational velocities in addition to a case with zero rotation. Results show that the normalized mean velocity profile is in good agreement with the universal law-of-the-wall and previous published data. Comparison with LES data indicated good agreement with Reynolds shear stresses and the normalized mean velocities in the case of a non-rotating cylinder. However, deviations were observed when rotation was applied. In order to ensure the quality of the numerical results a convergence study was performed. Special attention was paid to the near-wall region in order to capture all levels of the boundary layer.

Sammendrag

De fleste problemer som involverer viskøse strømninger er karakterisert ved turbulens. Ustabiliteter og store hastighetsgradienter forårsaker fluktuasjoner i strømningsfeltet. Tauede sonarer er utsatt for turbulens i grensesjiktet rundt kabelen. Problemer oppstår når kabelen roterer om sin egen akse på grunn av variabel strekkraft forårsaket av den slepende farkosten. Numeriske beregninger av en trykkdreven strømning langs en sylinder er gjort med den hensikt å undersøke det turbulente grensesjiktet rundt kabelen. I dette studiet er Reynolds Average Navier-Stokes (RANS) likningene benyttet i det numeriske verktøyet OpenFOAM for å beregne strømningsfeltet. Resultatene ble deretter brukt i en sammenlikningsstudie med data fra Large Eddy Simulation (LES).

Simuleringene ble utfør for to forskjellige Reynolds tall basert på skjærhastigheten; $Re_\tau = [240,\ 550]$. Sylinderen ble tilordnet to forskjellige rotasjonshastigheter i tillegg til et tilfelle der rotasjonen var lik null. Resultatene viste at den normaliserte gjennomsnittlige hastighetsprofilen var i god overensstemmelse med den universelle law-of-the-wall og tidligere publiserte data. Sammenlikninger med LES data indikerte at Reynolds skjærspenninger og den normaliserte gjennomsnittlige hastighetsprofilen stemte godt overens i det tilfellet av en ikke-roterende sylinder. På den annen side ble det observert avvik fra LES dataene der sylinderen roterte. For å sikre kvaliteten på de numeriske resultatene ble det utført konvergensanalyser. Det ble særlig tatt hensyn til området nært til sylinderoverflaten for å fange alle nivåene i grensesjiktet.

Content

List of figures

List of tables

Nomenclature

Abbreviations

APG	Adverse Pressure-Gradient
CFD	Computational Fluid Dynamics
CFL	Courant-Frederich-Levy
DIC	Diagonal Incomplete-Cholesky
DILU	Diagonal Incomplete-LU
DNS	Direct Numerical Simulation
FDM	Finite Difference Method
FEM	Finite Element Method
FPG	Favourable Pressure-Gradient
FVM	Finite Volume Method
LES	Large Eddy Simulation
OpenFOAM	Open Field Object And Manipulation
PBiCG	Preconditioned Bi-Conjugate Gradient
PCG	Preconditioned Conjugate Gradient
PDE	Partial Differential Equation
PIMPLE	Merged PISO-SIMPLE
PISO	Pressure Implicit with Splitting Opreator
RANS	Reynolds Average Navier-Stokes
S-A	Spalart-Allmaras
SIMPLE	Semi-Implicit Method for Pressure-Linked Equations
SST	Shear Stress Transport

Greek symbols

β	Clauser parameter, ratio of shear forces to pressure forces
Γ	Diffusivity coefficient
Γ_f	Diffusion through face f
δ	Boundary layer thickness
δ_{ij}	Kronecker delta function
ε	Rate of turbulent dissipation
ε_ν	Destruction term
κ	von Kámán constant
λ	Coefficient of bulk viscosity
ν	Kinematic viscosity
ν_t	Eddy viscosity/turbulent viscosity
$\tilde{\nu}$	Effective viscosity
ν_{eff}	Effective kinematic viscosity
ρ	Fluid density
σ	Empirical constant in Spalart-Allmaras model
τ	Total shear stress
τ_l	Laminar shear stress
τ_t	Turbulent shear stress
τ_w	Wall shear stress
ϕ	General quantity
ϕ_f	Flux through face f
Φ	Dissipation function
χ	Effective viscosity ratio
ψ	Weighting factor
ω	Specific dissipation
Ω	Control volume

Roman symbols

A_{ref}	Reference area
C_{df}	Frictional drag coefficient
C_{v1}	Empirical constant Spalart-Allmaras model
C^+	Integration constant
c_{b1}, c_{b2}, c_w	Empirical constant Spalart-Allmaras model
f	Face
F_f	Frictional force

f_g	Gravitational body force
f_{v1}	Viscous damping function
f_w	Non-dimensional destruction term
h	Enthalpy
H	Radius of control volume
k	Turbulent kinetic energy
k_t	Thermal conductivity/transport coefficient
L	Reference length
n	Normal vector
p	Pressure
p'	Corrected pressure
p^*	Initial pressure field
p^{**}	Corrected pressure
$\mathcal{P}_v$	Production term
Re_a	Reynolds number based on cylinder radius
Re_δ	Reynolds number based on boundary layer thickness
Re_τ	Reynolds number based on shear velocity
S	Magnitude of vorticity
S_f	Area vector through face f
T	Temperature
U	Mean velocity
U^+	Non-dimensional velocity
U_r	Radial velocity
U_θ	Circumferential velocity
$\overline{u_i u_j}$	Reynolds shear stress
u_τ	Shear velocity
u	Instantaneous velocity
u'	Fluctuating velocity
$\overrightarrow{V_f}$	Velocity through face f
$\vec{V}$	Velocity vector
V_∞	Free stream velocity
y^+	Non-dimensional distance to wall

1 Introduction

Turbulence is the state of fluid flow characterized by unpredictable and chaotic motions. It is one of the most challenging problems faced within the discipline of fluid dynamics. The nature of the flow are swirly motions forming eddies which vary in size, time and space. The path of the fluid particles are difficult to follow as oppose to laminar flow where they follow a smooth and orderly path in layers. For engineering application this type of flow is important, consequently scientists have invested a great deal of effort in understanding the phenomenon of turbulence. The characteristic eddies exist in a range of scales, where energy is transferred from the larger scales to the smaller, until it is dissipated through kinematic viscosity. Figure 1.1 illustrates the range of scales that occur in a turbulent flow. Kolmogorov formulated this into laws which pre-date the concept of the energy cascade [1]. In 1883 Osborne Reynolds performed an experiment illustrating the different states of fluid flow [2]. Dyed water was injected into a transparent pipe in which the main stream flowed. He observed that an increase in drag corresponded to the occurrence of turbulent flow. The change of the flow regime was quantified through a number, the Reynolds number, where the flow shifts from laminar to turbulent when a certain value is exceeded.

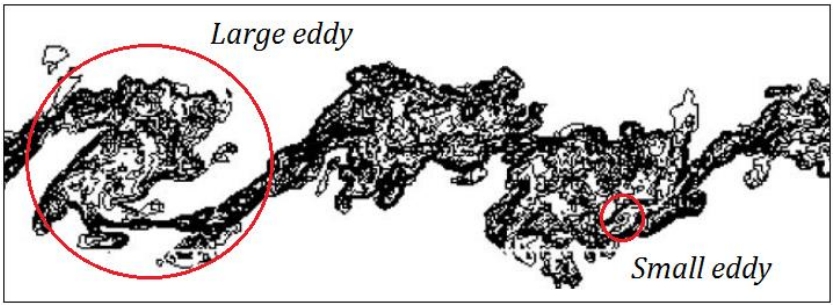

Figure 1.1: Eddies exist in a range of scales. Modified picture from [3].

In this thesis, pressure driven turbulent flow along a cylinder, with and without rotation, is studied utilizing numerical methods. The Reynolds Average Navier-Stokes (RANS) approach is applied to solve the flow field, providing a time-averaged solution to the Navier-Stokes equations when specific flow quantities are known. Flow along cylinders is of interest for several applications, including

marine pipelines, aircrafts and towed acoustic array systems. Towed acoustic array systems are used for detection, tracking and reporting of objects below the water surface. It is utilized both in the civilian and military industry mainly for oil and gas exploration and in antisubmarine warfare. The concept of the system is simple; an arrangement of thin cables, up to $10 - 12\ km$ in length, are towed behind a surface vessel or an underwater vehicle. Acoustic receivers, mounted on the cables, register sound pulses transmitted or reflected by objects [4].

When the cable is towed through water noise or unwanted acoustic signals is generated from the turbulent motions. Under normal operations this type of disturbances typically makes up 50% of the recorded noise at low frequencies (at less than $100\ Hz$) [5]. Occasionally, the cable also experiences variation in tension force due to the motion of the towing vehicle. The combination of the cable not being perfectly homogeneous, due to small asymmetries introduced during manufacturing, and variable tension causes the cable to rotate around its longitudinal axis. The rotation modifies the boundary layer and consequently also the noise.

1.1 Towed acoustic arrays

Towed acoustic arrays may be classified as passive or active systems, depending on how the recorded sounds are generated. An active system consists of transmitters and receivers, as depicted in Figure 1.2. The transmitters are placed below the surface vessel generating sound pulses which propagates through the water. When the sound pulses hit an object, or the seabed, they are refracted and an echo is generated. The echo is recorded by the receivers, or hydrophones, placed along the cables. The acoustic signals are then sent back to the surface vessel where they are processed. Passive systems are similar, but do not make use of transmitters. Instead, the hydrophones are used to detect sound generated from other objects, e.g. propeller noise or submarine navigation systems. The passive systems are mainly used by the military industry where it is vital not to reveal ones position. Towed acoustic arrays were adopted for the first time during World War I. In 1917, at the U.S. Navy Experimental Station, Dr. Hays developed a towed array system that was meant to detect submarines. The system was called Eal Sonar System [6].

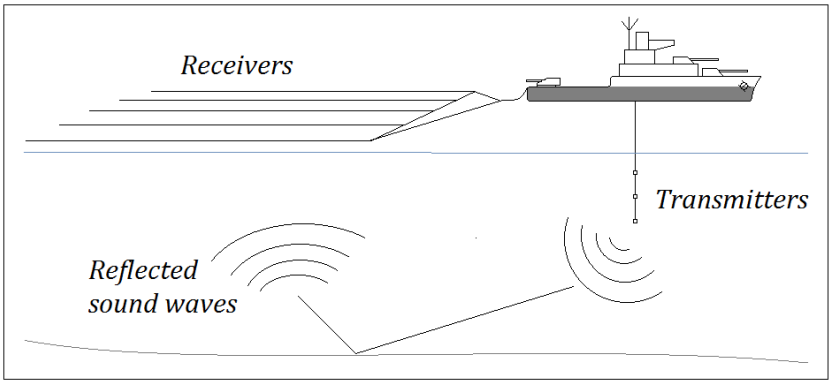

Figure 1.2: Active array system.

1.2 Computational Fluid Dynamics (CFD)

Computational Fluid Dynamics (CFD) is a discipline within fluid dynamics that apply numerical models and algorithms to describe the flow field. The governing equations for most numerical software are the Navier-Stokes equations which describe the motion of viscous fluids. Numerical tools in engineering application have become more popular over the last decades as the computer capacity allows for more complex computations. Compared to the classical methods (experimental and theoretical), CFD is more cost-effective and flexible because it allows sampling of desired flow quantities at any point in the fluid domain.

The approach of solving the turbulent flow field without any simplification of the Navier-Stokes equations is called Direct Numerical Simulation (DNS). The whole range, from the largest to the smallest dissipative scales, is solved directly. This is a computational expensive task and calls for high performance computers. In practice this method is only applied to flows with low Reynolds number. The Large Eddy Simulation (LES) approach does not resolve the full range of scales. As the name implies, it only solves for the largest scales occurring in a turbulent flow, which makes it less computational expensive compared to DNS. De Villiers [7] explain that the smaller eddies are believed to be more or less universal and are modelled using a sub-grid scale. He also points out that LES is justified because the largest scales contain the most energy and transports most of the conserved fluid properties. In the RANS approach the governing equations are simplified by time-averaging. This is equivalent to carry out a high number of identical experiments and then take the mean of the flow quantities at the same time instant. RANS is the least computational expensive method of the three approaches mentioned here and is capable of solving flows over complex geometries at high Reynolds number.

1.3 Flow along a cylinder

Most physical problems involving viscous fluid flows are characterized by turbulence. Instabilities and large velocity gradients generate fluctuations in the flow field. From a physical perspective, the development of a boundary layer along a cylinder is in many situations similar to the case of flow over a flat plate. Consider the case of a cable towed through water; a relative thick axisymmetric turbulent boundary layer is formed along the cable. Flows experiencing axial symmetry have been the topic of many articles. Cham & Head [8] investigated the turbulent boundary layer of a rotating cylinder. They observed that the only evidence of three-dimensionality laid in the destabilizing effect of a rotating cylinder. By transforming the coordinate system to a set of axes rotating with the cylinder, the boundary layer downstream approximated closely to a two-dimensional condition.

The terms "axisymmetric boundary layer" and "cylindrical boundary layer" are used interchangeably in articles to describe the two-dimensional behaviour. Obtaining complete axial symmetry in experimental methods is difficult because of physics that are not controllable when the boundary layer becomes thick. Lueptow [9] suggest that the term "cylindrical" is more suited in this case. His experiments of a cylinder in axial flow showed that the curvature in the transverse direction resulted in a higher frictional coefficient and a "fuller" velocity profile than in the case of a flat plate. For large cylinder radii (compared to the boundary layer thickness) the mean velocity profile was identical to the planar case, but when the radius became small the deviations increased. Measurements that were available for cylindrical boundary layers suggested that the distribution of the turbulent quantities were somewhat different from the planar case. The mean velocity profile on cylinders of various diameters was also investigated experimentally by Willmarth et. al. [10]. It was found that the profile was well described by the universal *law-of-the-wall*. The axisymmetric turbulent boundary layer was also the topic of the study by Afzal & Narasimha [11]. They examined available experimental data, including the data of Willmarth et. al., and found that the boundary layer was well described by the classical form of law-of-the-wall, given that the Reynolds number was of sufficient size to develop a fully turbulent boundary layer. Behaviour quantities relevant for the performance of towed arrays were investigated by Tutty [12]. Numerical calculations was carried out for flow along a cylinder at a Reynolds number ranging from 300 to $5 \cdot 10^4$ and subsequently compared to experimental data. The results showed good agreement with those from experiments. He also pointed out that strong turbulent flow only occurs near the cylinder surface and that turbulence was weak in the rest of the boundary layer.

Marschall et. al. [13] and Potter et. al. [14] address the problem of increased turbulent flow noise for decreasing diameter of the towed array at a given tow speed. The motivation for decreasing array-diameter is related to weight and handling problems during launching and recovering. Marschall et. al.

discussed a marine seismic survey test conducted in the Antarctic using a non-constant diameter array. The hydrophones were placed in a hydrodynamically housing creating a laminar boundary layer, rather than a turbulent, resulting in reduced turbulent flow noise. Potter et. al. explained that conventional towed arrays usually have a diameter of $40 - 80\,mm$ and a weight of approximate $1\,kg/m$. As the length of the cables are in the order of $15\,km$ the overall weight becomes substantial. Because of this, specialized ships are required to operate the system. It was suggested that a drastic reduction in the overall diameter to below $16\,mm$ may produce acceptable results with respect to turbulent flow noise. Other studies related to flow noise around seismic cables are found in [15] and [16]. The problem of flow noise is not explicitly the topic of this thesis, but reference is made as the performance of the towed array is limited by the noise generation.

1.4 Introduction to OpenFOAM

This chapter is a short introduction to the basic concepts of the program OpenFOAM (Open Field Operation And Manipulation). OpenFOAM [17] is a free open source software for numerical calculations of flow fields. The basis of the program is a C++ library which is divided into *solvers* and *utilities*. The solvers are designed to solve specific problems within continuum mechanics, and the utilities are used for pre- and post-processing of data. OpenFOAM is run through commands in a terminal window that requires a Linux operating system. For Windows users it is possible to install visualization software and run Linux as a guest operating system. The program applies for a broad range of fluid dynamic problems such as compressible/incompressible flows, multiphase flows, combustion, particle methods and electromagnetics. It offers many opportunities because it allows running standard or customized solvers. The main structure of OpenFOAM is illustrated in Figure 1.3.

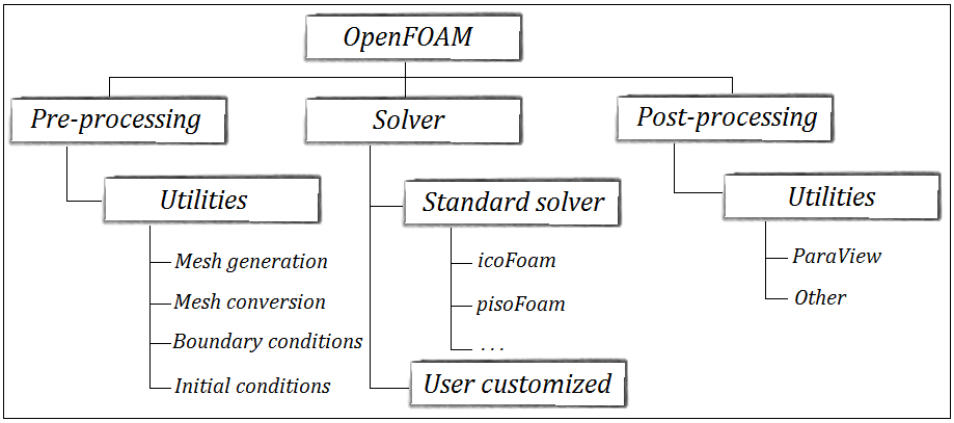

Figure 1.3: The structure of OpenFOAM.

The reason for its success might be due to its broad application area and the fact that the code is free and open. Even though the software is popular it has some disadvantages. Lysenko et.al [18] points out the most crucial as:

- The lack of default settings.
- The large amount of different numerical schemes and models, which is a disadvantage for inexperienced users.
- The lack of documentation and references makes it difficult to validate and verify the quality of capabilities.

Upon solving a problem in OpenFOAM one has to create a case directory. The case directory has to contain a minimum of three subdirectories; `constant`, `system` and `0`. The `constant`-directory contains the discrete representation of the model, fluid domain and physical properties of the flow. The `system`-directory contains information about the solver being used. Initial conditions for e.g. pressure and velocity are defined in the `0`-directory. Figure 1.4 illustrates the structure of a case-directory in OpenFOAM.

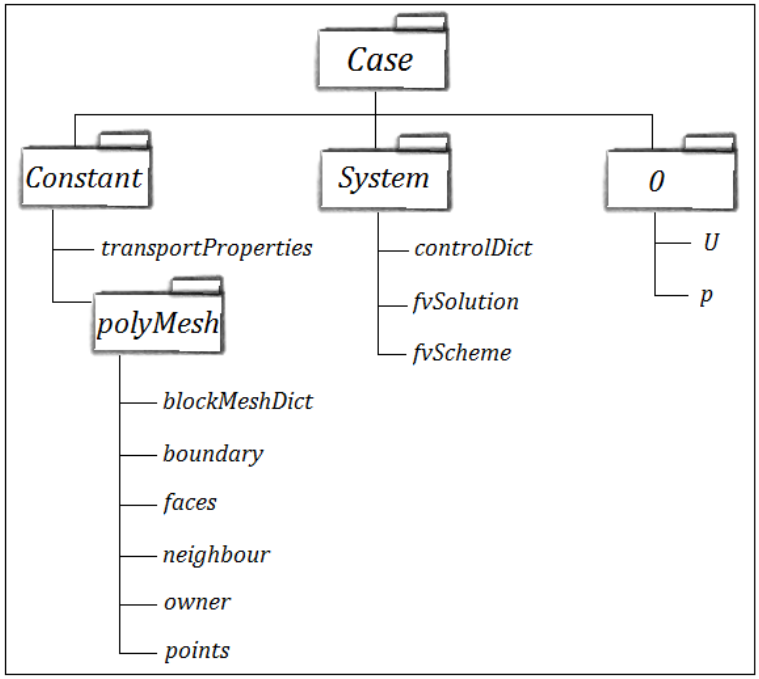

Figure 1.4: Structure of case directory in OpenFOAM.

2 Governing equations

This section is mainly based on White [19] and Cebeci & Cousteix [20]. In order to mathematically describe the motion of the fluid a set of equations has to be established. In fluid dynamics the classical laws of conservation is applied:

- Conservation of mass, the governing equation is called *the continuity equation*.
- Conservation of momentum, this relation is based on *Newton's second law*.
- Conservation of energy, the governing equation is called *the energy equation*.

All of these equations are usually referred to as the Navier-Stokes equations. Here, three unknowns are present; the velocity $\vec{V}$, thermodynamic pressure p and absolute temperature T. In addition density, enthalpy and transport properties will influence the flow, but by assuming a fluid of homogeneous composition only $\vec{V}$, p and T has to be considered. The following section contains a description of the governing equations followed by simplifications. The equations are presented on differential form which means they denote influences on a unit volume, or control volume. This allows us to study a certain amount of fluid flowing in and out of a system, Figure 2.1 illustrate such a system.

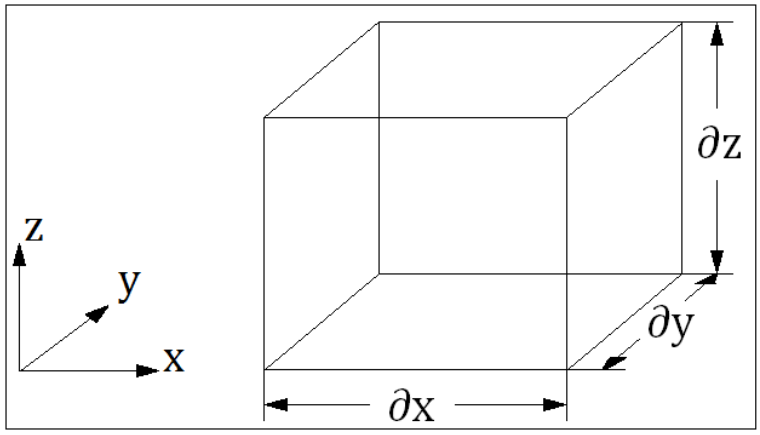

Figure 2.1: Control volume.

2.1 Conservation of mass (continuity equation)

The continuity equation states that the rate of mass going out of a system is equal to the rate of mass going in. In other words, no mass is neither created nor destroyed inside the control volume. On general form the continuity equation may be written:

$$\frac{\partial \rho}{\partial t} + \nabla \cdot \left(\rho \vec{V}\right) = 0 \qquad \textbf{(2.1)}$$

for a three-dimensional flow in x-, y- and z-direction. Here, ρ is the density of the fluid, $\partial\rho/\partial t$ is the rate of change of density and $\vec{V} = [u, v, w]$ is the velocity vector. ∇ is the differential operator; $\nabla = \partial(\,)/\partial x + \partial(\,)/\partial y + \partial(\,)/\partial z$.

2.2 Conservation of momentum (Newton's 2nd law)

This law states that, within a control volume, the amount of momentum remains constant:

$$\frac{\partial \vec{V}}{\partial t} + \vec{V} \cdot \left(\nabla \vec{V}\right) = f_g - \frac{1}{\rho}\nabla p + \nabla \cdot \left(\nu \nabla \vec{V} + \delta_{ij}\lambda \nabla \cdot \vec{V}\right) \qquad \textbf{(2.2)}$$

for a three dimensional flow in x-, y- and z-direction. f_g represents gravitational body forces and ∇p is the pressure-gradient. The last term on the right hand side represents viscous forces where ν is the kinematic viscosity and λ the coefficient of bulk viscosity which is associated with volume expansion. δ_{ij} is the Kronecker delta function:

$$\delta_{ij} = \begin{cases} 1 & if \;\; i = j \\ 0 & if \;\; i \neq j \end{cases}$$

2.3 Conservation of energy

Conservation of energy is based on the first law of thermodynamics which states that the energy within a control volume remains constant:

$$\rho \frac{Dh}{Dt} = \frac{Dp}{Dt} + \nabla \cdot (k_t \nabla T) + \Phi \qquad \textbf{(2.3)}$$

where h is the fluid enthalpy, k_t is thermal conductivity (also called the transport coefficient) and ∇T is the temperature gradient, Φ is called the dissipation function.

2.4 Governing equation for incompressible flow

The fluid is incompressible when the variations in density are so small that it can be neglected, i.e. $\partial\rho/\partial t = 0$. Equation (2.1) is simplified to:

$$\nabla \cdot \vec{V} = 0 \tag{2.4}$$

With the assumption of constant density λ disappear from the momentum equation. In addition, assuming constant viscosity and neglecting gravitational body forces equation (2.2) simplifies to:

$$\underbrace{\frac{\partial \vec{V}}{\partial t}}_{Temporal\ term} + \underbrace{\vec{V} \cdot \left(\nabla \vec{V}\right)}_{Convective\ term} = -\frac{1}{\rho}\nabla p + \underbrace{\nabla \cdot \left(\nu \nabla \vec{V}\right)}_{Diffusion\ term} \tag{2.5}$$

With the assumption of constant viscosity and density the equations for continuity and momentum becomes uncoupled from the energy equation and, hence, the temperature, T. The consequence of this is that one may solve continuity and momentum for V and p and later, if desired, solve for temperature. The body forces, in the momentum equation, are neglected since the momentum- and energy equation is uncoupled.

3 Turbulence modelling

Turbulent flow is characterised by the ability to mix substances introduced in to the fluid and dissipate energy. Without turbulence, the substances would have followed in smooth and orderly layers and slowly diffuse by kinematic viscosity. Tennekes et. al. [21] explain that turbulent flow is always three-dimensional; the flow contain high levels of random fluctuations which cannot be maintained if the velocity-fluctuations are two-dimensional since a mechanism called vortex stretching is absent in a two-dimensional flow.

Because eddies occur randomly in time and space analysis of turbulent flow becomes a complex task. Investigation of turbulent flow then requires statistical methods. The most widely used method is *Reynolds decomposition* where the instantaneous flow properties are divided into a mean and fluctuating part [22]. A typical record of turbulent behaviour is depicted in Figure 3.1, which illustrates measurements of e.g. wind velocity over a period of time. Here, the instantaneous velocity, u, is divided into a mean part and a fluctuating part; $u = U + u'$, where U is the mean part and u' is the fluctuating part.

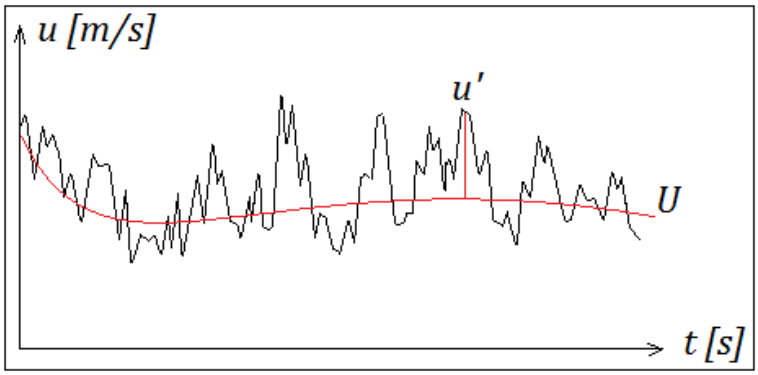

Figure 3.1: Record of wind velocity.

3.1 Plus units

Plus units are non-dimensional variables used in turbulent boundary layer analysis. The use of non-dimensional parameters enables to more easily compare results. The variables of interest are:

$$y^+ = \frac{u_\tau r}{\nu}, \qquad U^+ = \frac{U}{u_\tau}, \qquad Re_\tau = \frac{u_\tau H}{\nu} \tag{3.1}$$

where y^+ is the non-dimensional distance from the wall, U^+ is non-dimensional velocity and Re_τ is the Reynolds number based on shear velocity $u_\tau = \sqrt{\tau_w/\rho}$. τ_w is the shear stress at the wall and H is the radius of the control volume. In the literature, y^+ and U^+ are also referred to as wall-coordinates.

3.2 Turbulent boundary layer

Consider a flow over a flat plate with a uniform velocity profile as in Figure 3.2 at position 1. Close to the plate, fluid particles tend to stick to the surface where the velocity becomes zero. This phenomenon, referred to as no-slip, will in turn affect the adjacent particles. The region where the fluid particles are affected by no-slip is called the boundary layer, as illustrated at position 2 in Figure 3.2. After some distance the flow becomes unstable and eddies are formed. At position 3 a turbulent boundary layer is formed. The thickness of the boundary layer is denoted δ. The presence of a wall, or boundary, makes the structure and behaviour of the turbulent boundary layer different from free shear flows. In contrast to the fully turbulent region of the flow where the effect of kinematic viscosity is negligible this is present and important close to a wall. The production and dissipation of turbulent energy peaks near the wall where more than 30% of the total production and dissipation takes place.

The turbulent boundary layer is commonly treated as a composite layer consisting of an inner- and outer region. The inner layer is about 15% of the boundary layer thickness and is further divided into a linear sublayer, buffer layer and log-law region. The outer layer is about 85% of the total boundary layer thickness [20]. There is not fixed limit on where the outer layer starts and the inner layer stops, in some cases these overlap each other.

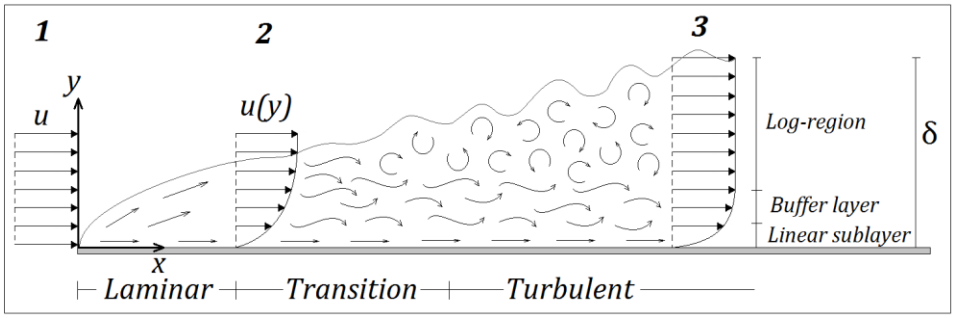

Figure 3.2: Formation of laminar and turbulent boundary layer. Modified picture from [23].

Close to an impermeable wall, in the inner layer, the velocity profile for a fully turbulent boundary layer can be non-dimensionalized in terms of plus units. The resulting curve takes a characteristic form which is similar for different Reynolds number. The universal curve is referred to as *law-of-the-wall*, or the *log-law*, where the velocity at a point is proportional to the logarithm of the non-dimensional distance from the wall y^+. The law-of-the-wall was first proposed by von Kármán in 1930 [24] and has shown valuable for predictions of turbulent flow behaviour. For instance, the presence of a universal law formed the basis for the Preston tube [25] which is used in measurement of wall skin friction. At a distance far enough from the wall where kinematic viscosity is negligible the velocity can be approximated:

$$U^+ = \frac{1}{\kappa}\ln(y^+) + C^+ \qquad \textbf{(3.2)}$$

where κ is the von Kármán constant, usually equal to 0.41, C^+ is an integration constant, generally taken as 5.1 and ln is the natural logarithm. Closer to the wall the velocity varies linearly:

$$U^+ = y^+ \qquad \textbf{(3.3)}$$

The existence of the log-law has been confirmed by many since von Kármán's discovery. Some examples are; Nikuradse [26], Prandtl [27] and Schlichting [28]. A typical representation of the velocity distribution in the inner layer is given by Bernardini et. al [29]:

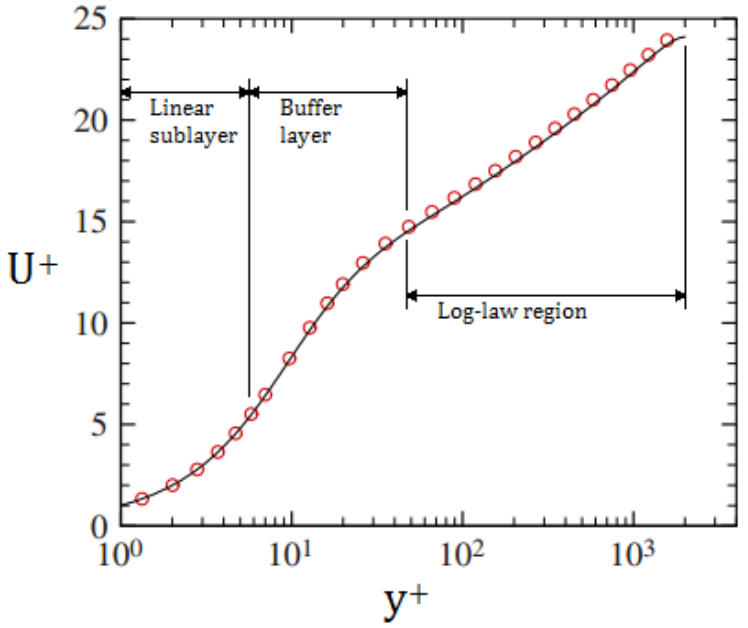

Figure 3.3: The inner layer of a turbulent boundary layer. Comparison between DNS data for two different Reynolds number.

In the inner layer the mean velocity distribution is determined by the wall shear stress τ_w, viscosity ν and the distance from the wall y with the assumption of linear variation of τ_w with increased y. Hence, it becomes independent of the condition in the outer layer. In the linear sublayer, defined in the range of $0 < y^+ < 5$, the velocity follows the approximation given in equation (3.3). The log-law region is entered about $y^+ \approx 40$ where the velocity is described by equation (3.2) [3]. The buffer layer is defined in the range of $5 < y^+ < 40$. Neither equation (3.2) nor (3.3) is valid in this region. More details on the characteristics of the turbulent boundary layer with zero pressure-gradient are given by Klebanoff [30]. In the outer layer the velocity profile have a slight deviation from the log-law. Coles [31] observed an additional wake-like velocity component and formulated what is referred to as *law-of-the-wake*. In Figure 3.4 the law-of-the-wake starts to emerge at $y^+ = 300$.

3.3 Effect of pressure-gradient

The presence of a pressure-gradient has an effect on the turbulent statistics in terms of mean velocity distribution, shear stress and turbulence production. The pressure-gradient is usually classified into Adverse Pressure-Gradients (APG) where the flow experience a positive pressure-gradient ($dp/dx > 0$) and Favourable Pressure-Gradients (FPG) where the flow is exposed to a negative pressure-gradient ($dp/dx < 0$) (x denotes the streamwise direction). In FPG flows the gradient of the velocity outside the boundary layer is positive and leads to an accelerating flow. APG flows cause a negative velocity gradient outside the boundary layer and leads to a deceleration. An accelerating flow causes the boundary layer to be thinner and stabilized, but a deceleration gives a thicker boundary layer and in some cases lead to flow separation [32]. If the acceleration of the free-stream is large, the turbulence does not have much time to respond. When this happens, the turbulence fluctuations are nearly constant and the free-stream velocity increases. The velocity distribution is characterized by a constant value of the parameter β:

$$\beta = \left(\frac{\delta}{\tau_w}\right)\left(\frac{\partial p}{\partial x}\right) \qquad \textbf{(3.4)}$$

which represents the ratio of shear forces to pressure forces in a section of the boundary layer. Here, δ is the boundary layer thickness. This parameter was first suggested by Clauser [33] in 1954. Spalart & Watmuff [34] studied the effect of pressure-gradient on the turbulent boundary layer. They found that the velocity profile in the buffer- and lower log-layer shifted up when the flow was exposed to FPG and correspondingly a shift downwards occurred for APG. These results were similar to the findings of Nagano et. al. [35]. More recently, Harun [36] investigated the effect of APG and FPG on the turbulent boundary layer. His results confirm the findings by Spalart & Watmuff, and found that the shift in velocity was independent of the Reynolds number, see Figure 3.4. The Clauser parameter β was varied while the Reynolds number was kept constant.
The APG increases the turbulence production close to the wall and in the outer region. Correspondingly the FPG decreases the turbulence production. Skåre & Krogstad [37] explain that the high production in the APG flow is due to the very high turbulent shear stresses found in the outer region. Boundary layers undergoing strong FPG may take a laminar-like form. This phenomenon is called *relaminarization* or *reverse transition*. Especially for the velocity profile and the skin friction this is evident and is due to loss of turbulent transport close to the wall [32]. Relaminarization is investigated by many, e.g. Patel & Head [38] Blackwelder & Kovasznay [39] Badri Narayanan & Ramjee [40] and Launder [41].

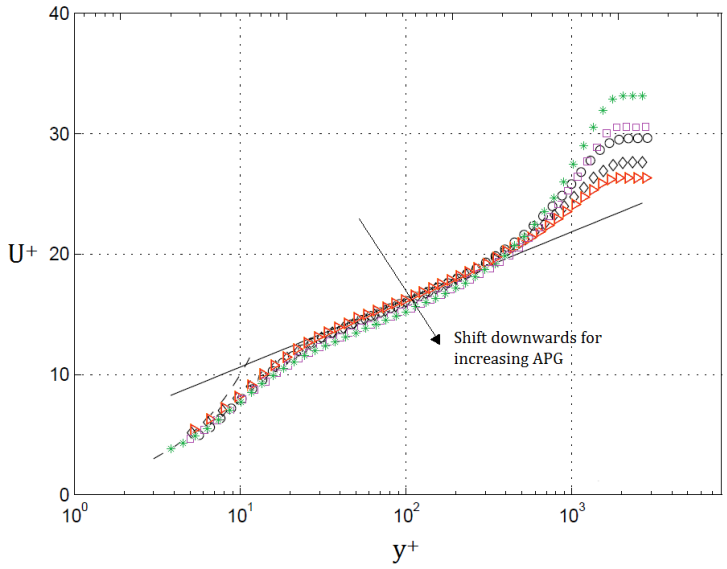

Figure 3.4: Effect of increased APG on velocity profile. (▷) $\beta = 0$, (◊) $\beta = 0.91$, (○) $\beta = 1.67$, (□) $\beta = 2.81$, (☆) $\beta = 4.54$. After Harun [36].

3.4 Reynolds Average Navier-Stokes (RANS) equations

Turbulent flow is characterized by a high degree of fluctuations and almost an infinite range of scales. Solving the Navier-Stokes equations for all these scales will be a comprehensive task. A solution is to reduce the number of scales by applying Reynolds decomposition where the instantaneous variables are separated into a fluctuating part and a mean part.

$$u = U + u', \qquad v = V + v', \qquad w = W + w', \qquad p = P + p'$$

Here u, v, w, p are the instantaneous values, U, V, W, P are the mean values and u', v', w', p' are the fluctuating part. The instantaneous variables in the Navier-Stokes equations (equation (2.4) and (2.5)) are replaced by the mean and fluctuating part and simplified through a process called Reynolds averaging where the unsteadiness of the flow is removed through time-averaging. The details of the procedure are not given here, and reference is made to Cebeci & Cousteix [20] and Durbin & Reif [3]. On component form, the result is the following equations valid for incompressible flows:

$$\frac{\partial U}{\partial x} + \frac{\partial V}{\partial y} + \frac{\partial W}{\partial z} = 0 \qquad \textbf{(3.5)}$$

$$\frac{\partial U}{\partial t} + U \cdot \nabla U = -\frac{1}{\rho}\frac{\partial P}{\partial x} + \nabla \cdot (\nu \nabla U) - \frac{\partial}{\partial x}\left(\overline{u'^2}\right) - \frac{\partial}{\partial y}(\overline{u'v'}) - \frac{\partial}{\partial z}\left(\overline{u'w'}\right) \quad \textbf{(3.6)}$$

$$\frac{\partial V}{\partial t} + V \cdot \nabla V = -\frac{1}{\rho}\frac{\partial P}{\partial y} + \nabla \cdot (\nu \nabla V) - \frac{\partial}{\partial x}\left(\overline{v'u'}\right) - \frac{\partial}{\partial y}\left(\overline{v'^2}\right) - \frac{\partial}{\partial z}\left(\overline{v'w'}\right) \quad \textbf{(3.7)}$$

$$\frac{\partial W}{\partial t} + W \cdot \nabla W = -\frac{1}{\rho}\frac{\partial P}{\partial z} + \nabla \cdot (\nu \nabla W) - \frac{\partial}{\partial x}\left(\overline{w'u'}\right) - \frac{\partial}{\partial y}\left(\overline{w'v'}\right) - \frac{\partial}{\partial z}\left(\overline{w'^2}\right) \quad \textbf{(3.8)}$$

Equation (3.5) is equivalent to conservation of mass and (3.6)-(3.8) corresponds to conservation of momentum. The bar denotes time-averaged velocity. The difference between these equations and the equations governing laminar flow are the Reynolds shear stresses $\overline{u_i' u_j'}$ appearing on the right hand side of equation (3.6)-(3.8). Whereas the solution of laminar flow can be treated purely mathematical, problems involving turbulent flows has to be treated both mathematical and physical because there are no exact theories relating the Reynolds shear stresses to the dependent variables. Some important features of the RANS equations; they are non-linear and coupled. The non-linearity is due to the convection term in the momentum equation since they contain the velocity squared. The coupling is due to the velocity appearing in both equations; hence they cannot be solved separately.

3.5 Turbulent boundary layer equations

Further simplifications of the Navier-Stokes equations are possible when the ratio of the boundary-layer thickness δ to a reference length L is sufficiently small. In this way, terms that are smaller than a factor of δ/L are negligible. The resulting equations are called boundary-layer equations, and for three-dimensional incompressible flows we have:

$$\frac{\partial U}{\partial x} + \frac{\partial V}{\partial y} + \frac{\partial W}{\partial z} = 0 \quad \textbf{(3.9)}$$

$$U \cdot \nabla U = -\frac{1}{\rho}\frac{\partial P}{\partial x} + \nabla \cdot (\nu \nabla U) + \frac{\partial}{\partial y}(-\overline{u'v'}) \quad \textbf{(3.10)}$$

$$\frac{\partial P}{\partial y} = 0 \quad \textbf{(3.11)}$$

$$W \cdot \nabla W = -\frac{1}{\rho}\frac{\partial P}{\partial z} + \nabla \cdot (\nu \nabla W) + \frac{\partial}{\partial y}\left(-\overline{v'w'}\right) \quad \textbf{(3.12)}$$

The total shear stresses appearing on the right hand side of the momentum equation in x-direction can be written:

$$\tau = \tau_l + \tau_t = \nu \frac{\partial U}{\partial y} + (-\overline{u'v'}) \quad \textbf{(3.13)}$$

where τ_l is the laminar, or viscous, contribution to the shear stresses and τ_t is the turbulent contribution which corresponds to the Reynolds stress. Similar argument is valid for z-direction. In the laminar sublayer the turbulent shear stresses are negligible small because in most cases it is assumed that u', v' and w' is equal to zero at a solid surface.

3.6 Turbulence models

Consider the RANS equations ((3.5)-(3.8)) The unknown variables are U, V, W, P and the Reynolds shear stresses $\overline{u_i'u_j'}$ which means that there are more unknown than equations – they do not form a closed set of soluble equations. To overcome this, turbulence models are used in order to express the Reynolds shear stresses in known variables. The purpose of applying turbulence models is to add further equations such that the equation-set is closed. These models are generally based on empiricism and curve fitting from experimental data, and are therefore restricted to certain flow phenomena. Because kinematic viscosity is of less importance in turbulent flows an eddy viscosity ν_t, representing transport and dissipation of energy at smaller scales, is used in the prediction of the flow. For the problem in question, the Spalart-Allmaras model is applied, but a short description of other commonly used models are included as well.

3.6.1 The Spalart-Allmaras model

The Spalart-Allmaras model, henceforth termed S-A, is a one-equation turbulence model for compressible/incompressible flows. The model is based on the earlier model of Baldwin & Barth [42] and was originally developed for aerodynamics flows. Its formulation was derived using empirical relations, dimensional analysis and Galilean invariance. The transported variable is an effective viscosity $\tilde{\nu}$ which is assimilated to the eddy viscosity.The advantage of just one equation is that it becomes less memory-intensive than other models using two equations because it does not require as fine grid resolution as e.g. the $k-\varepsilon$ model. The transport equation for this model is written:

$$\frac{\partial \tilde{\nu}}{\partial t} + \nabla \cdot \left(\tilde{\nu}\vec{V}\right) - \frac{1}{\sigma}\nabla \cdot [(\nu + \tilde{\nu})\nabla\tilde{\nu}] = \mathcal{P}_\nu - \varepsilon_\nu + \frac{1}{\sigma}c_{b2}|\nabla\tilde{\nu}|^2 \qquad \textbf{(3.14)}$$

On the left hand side of equation (3.14) the temporal-, convective- and diffusive term is recognized. On the right hand side we have production $\mathcal{P}_\nu$, destruction ε_ν and transport respectively. The production term is written $\mathcal{P}_\nu = c_{b1}S\tilde{\nu}$, where S is the vorticity magnitude of the mean flow field. The turbulence production is controlled by the vorticity created at the wall, and is hence important for near-wall flows. The destruction term takes the form $\varepsilon_\nu = c_{w1}f_w(\tilde{\nu}/y)^2$, where f_w is a non-dimensional destruction function and y is the distance to the wall. When $\sigma = 2/3$ the coefficients c_{b1} and c_{b2} equals 0.1355 and 0.622 respectively. The indices b and w stands for *basic* and *wall*. The destruction term is related to inviscid blocking which is due to turbulent fluctuations are damped by the local pressure in the vicinity of a wall. The Boussinesq eddy viscosity assumption is used in the evaluation of the Reynolds shear stresses, where the eddy viscosity is obtained from:

$$\nu_t = \tilde{\nu} f_{v1} \qquad \textbf{(3.15)}$$

The viscous damping function is given by:

$$f_{v1} = \frac{\chi^3}{\chi^3 + C_{v1}^3} \qquad \textbf{(3.16)}$$

where

$$\chi = \frac{\tilde{\nu}}{\nu} \qquad \textbf{(3.17)}$$

ν is the kinematic viscosity, the coefficient C_{v1} is typically 7.1 and f_{v1} is a damping function. With the Boussinesq assumption the Reynolds stresses are considered proportional to the rate of strain tensor. The model performs well on

flat plate boundary layers and two-dimensional mixing layers, but fails in complex flows such as jet flows and separated flows. Generally, the S-A model has shown inappropriate to predict the relaminarization phenomenon, but performs well for fully turbulent computations [43]. For further information about the details of the S-A model, please see Spalart & Allmaras [44].

3.6.2 The $k-\varepsilon$ model

The purpose of the $k-\varepsilon$ model is to predict an eddy viscosity from velocities and time-scales.The model contain two equations where the transported variables are the turbulent kinetic energy k and the rate of turbulent dissipation ε. A number of variations of the $k-\varepsilon$ model exist, and what is referred to as the standard $k-\varepsilon$ model was derived by Jones & Launder in 1972 [45]. This model is applicable for problems with high Reynolds number. However, modifications, such as the Launder-Sharma and Chien, are designed to handle low-Re problems. For further details on low-Re models reference is made to Patel [46]. The $k-\varepsilon$ model is the most widely used turbulence model. Frei [23] justify this popularity by pointing out the good convergence rate and relative low memory requirement of the model. Further he explains that the model performs well for external flows around complex geometries, but is not suited for jet flows or problems where the flow exhibit strong curvature or adverse pressure-gradients.

Problems arise when considering the near-wall region. The model fails to predict the supressing of turbulent mixing that takes place in this region [3]. For situations where the near-wall region is important this deficiency will have serious consequences for the prediction of skin friction. A method to overcome this shortcoming is to abandon the $k-\varepsilon$ in the near-wall region and apply a set of prescribed profiles called wall functions. In this way, the $k-\varepsilon$ is applied in the free-stream region and the wall functions are used in the near-wall region.

3.6.3 The $k-\omega\ SST$ model

The abbreviation SST stands for “Shear Stress Transport” and was proposed by Menter in 1994 [47]. This is a modification of the standard $k-\omega$ which solves for the turbulent kinetic energy k and the specific dissipation ω. A shortcoming of the $k-\omega$ model is that the shear stresses have a tendency of being overestimated; this is fixed in the $k-\omega\ SST$ model. The advantage of this model is that it apply the $k-\omega$ formulation in the boundary layer and switch to a $k-\varepsilon$ in the free stream region making it applicable for high- and low-Re problems.

4 Computational method

The process of performing numerical calculations can be divided into three phases; pre-processing, running the solver and post-processing. Pre-processing involves definition of the fluid domain, discretization and definition of boundary- and initial conditions. This is typically the most time-consuming phase as it generally includes dependence-study of different parameters and domain on the solution. The choice of solver depends on the flow problem. If the fluid is incompressible, a solver intended for incompressible flows should be chosen, or, if the flow is compressible a different solver should be applied. Visualization and interpretation of results obtained from the numerical simulation are performed in the post-processing phase. The bulk of this section is based on the book by Versteeg & Malalasekera [48].

4.1 Discretization

The fluid domain cannot be infinite, numerically this would be impossible to solve. We have to restrict the problem to a certain amount of fluid. The chosen amount of fluid is referred to as the computational domain. In order to mathematically describe the fluid flow the computational domain and the governing partial differential equations (PDE) have to be discretized. Discretization is the description of a continuous system by discrete entities, and is divided into temporal- and spatial discretization. Spatial discretization involves breaking up the computational domain into finite number of elements called cells. The governing PDEs are discretized both in time and space in order to express the discrete solution of the flow field. The PDEs are then transformed into sets of algebraic equations. There exist numerous of discretization methods, some examples are the Finite Difference Method (FDM), Finite Element Method (FEM) and Finite Volume Method (FVM).

In the FDM the governing equations are replaced by series expansions where the most common procedure is to employ Taylor series. The more terms included the more accurate the solution, but the drawback is increased complexity and number of discrete nodes. The FDM is advantageous for simple geometries and can be applied to any cell type. In the FEM the equations are integrated over a two-dimensional or three-dimensional element and multiplied by a weighting factor. OpenFOAM employ the FVM which is the most widely used. The method is based on volume integrals, where the governing equations are integrated over a volume element.

4.1.1 Domain discretization

In the FVM the computational domain is divided into three-dimensional cells, and all the cells within the domain constitute what we call the mesh, or grid. There are two main grid categories; co-located and staggered. In the co-located grid all flow quantities, such as pressure and velocity, are stored at a single point in the cell centre (Figure 4.1 a)). The velocities are used in the calculation of fluxes through the cell surface. For co-located grids, the velocities are then interpolated from the cell centre to the cell surface. The advantage of this is the number of coefficients that has to be calculated and stored is minimized and makes programming simpler [49]. The co-located type of arrangement also has an advantage for complex solution domains with slopes and discontinuities in the flow field. In the staggered grid arrangement the pressure is defined at the cell centre whereas the velocities are defined at the cell face (Figure 4.1 b)), meaning that there is no need for interpolation. In OpenFOAM the co-located grid type is adopted.

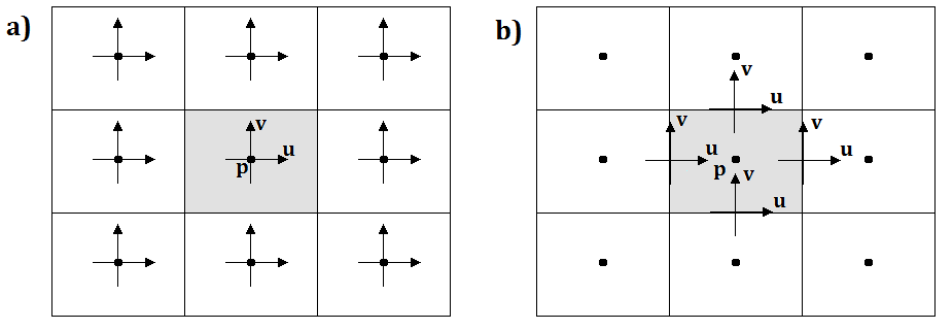

Figure 4.1: a) Co-located type of grid. b) Staggered type of grid.

4.1.2 Discretization of governing equations

The advantage of the integral form is that it can handle arbitrary shapes of the cells, making it flexible and suitable for complex geometries. Most spatial derivatives appearing in the governing equations are transformed to surface integrals by use of Gauss' theorem, or the divergence theorem. Consider a general quantity ϕ that may represent e.g. mass or velocity, Gauss theorem is written:

$$\int_{\Omega} (\nabla \cdot \phi)\, d\Omega = \int_{S} (\phi \cdot \mathrm{n})\, dS \qquad \textbf{(4.1)}$$

where Ω is control volume and S is the control surface. The product $\phi \cdot n$ is interpreted as the component of vector ϕ in the direction of n normal to the surface dS. This transformation is applicable for the continuity equation. To keep it consistent, consider the momentum equation for the general quantity ϕ:

$$\underbrace{\frac{\partial \phi}{\partial t}}_{Temporal\ term} + \underbrace{\nabla \cdot \left(\vec{V}\phi\right)}_{Convection\ term} = \underbrace{\nabla \cdot (\Gamma \nabla \phi)}_{Diffusion\ term} + \underbrace{S(\phi)}_{Source\ term} \qquad \textbf{(4.2)}$$

Here, Γ is the diffusivity coefficient, e.g. kinematic viscosity ν. All terms that cannot be written as temporal, convection or diffusion contribution is written as a source term. When applying Gauss' theorem, the momentum equation on integral form become:

$$\int_{\Omega} \frac{\partial \phi}{\partial t} d\Omega + \int_{S} \left(\vec{V}\phi\right) \cdot n \, dS = \int_{S} (\Gamma \nabla \phi) \cdot n \, dS + \int_{V} S(\phi) \, dV \qquad \textbf{(4.3)}$$

4.1.3 Linearization

The equation systems that govern particular scientific problems cannot be solved directly in an efficient way. Instead they are linearized and solved in sequences. In this case, the volume and surface integrals are linearized with an appropriate linearization scheme and evaluated as fluxes through the cell surface. As velocities are stored at the cell centre they have to be interpolated to the cell surface in order to calculate the net flux. The net flux is then the sum of integrals over six surfaces for a three-dimensional cell. The continuity equation is linearized as follows:

$$\int_{S} (\phi \cdot \mathrm{n}) \, dS = \sum_{f} \int_{S_f} (\phi \cdot \mathrm{n}) \, dS = \sum_{f} S_f \cdot \phi_f \qquad \textbf{(4.4)}$$

where S_f is the area vector pointing in the direction of the surface normal vector n at face f and ϕ_f is the flux through f(see Figure 4.2). The convection- and diffusion term of the momentum equation is linearized as follows:

$$\int_{S} \left(\vec{V}\phi\right) \cdot n \, dS = \sum_{f} \int_{S_f} \left(\vec{V}\phi\right) \cdot n \, dS = \sum_{f} S_f \cdot \left(\vec{V_f}\phi_f\right) \qquad \textbf{(4.5)}$$

$$\int_{S} (\Gamma \nabla \phi) \cdot n \, dS = \sum_{f} \int_{S_f} (\Gamma \nabla \phi) \cdot n \, dS = \sum_{f} \Gamma_f S_f \cdot (\nabla \phi)_f \qquad \textbf{(4.6)}$$

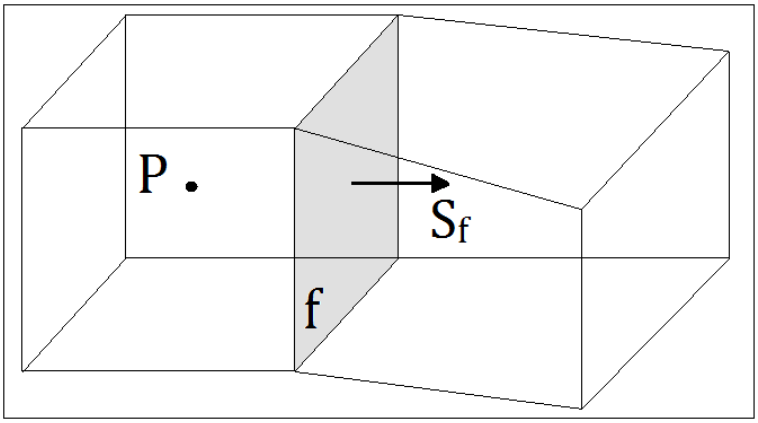

Figure 4.2: Three-dimensional cell with face f and surface area vector S_f. P is the cell centre where the flow quantities are stored.

4.1.4 Time discretization

Time discretization involves integrating the governing equation with respect to time t over a small interval Δt, let us say from t to $t + \Delta t$. For the problem in question the Crank-Nicholson method is applied. This combines the two first order Euler methods; backward and forward. A coefficient specified in the Crank-Nicholson method defines the weighting between the backward and forward method. When considering the general vector field ϕ, the time integral can be written [7]:

$$\int_t^{t+\Delta t} \phi(t)dt = \left[\psi\phi^{t+\Delta t} + (1-\psi)\phi^t\right]\Delta t \qquad \textbf{(4.7)}$$

where ψ is the weighting factor, $\phi^{t+\Delta t}$ represents the value of the dependent variable at the new time instant and ϕ^t represents the previous time. We have that $0 < \psi < 1$, where $\psi = 0$ corresponds to Euler backward and $\psi = 1$ corresponds to pure Crank-Nicholson. Because the Crank-Nicholson method is based on central differencing it is second-order accurate in time. With sufficient small time-step it is possible to achieve greater accuracy than with the Euler backward method.

4.1.5 Grid topology

A three-dimensional mesh may be built up by polyhedrals, pyramids, wedges or hexahedrals. In this study, structured hexahedral cells are placed in a polar domain (see Figure 4.3). Graded cells are useful in the sense of higher resolution close to an area of interest without having to increase the number of cells in the whole domain. The grading is set such that the cell closest to the cylinder surface is 10% of the cell furthest from the cylinder. The non-dimensional parameter y^+ describes the importance of turbulent to laminar influence in a cell and indicates how coarse/fine the mesh is for a particular case. To capture the laminar sublayer a requirement of $y^+ = 1$ is applied at the cylinder surface. Where y^+ spans from the cylinder surface to the outer boundary of the domain in radial direction.

Domain discretization is done through the `blockMesh`-utility in OpenFOAM, where the computational domain is decomposed into three-dimensional hexahedral cells. Each cell is built up by 8 vertices located at the corners of the hexahedron. `blockMesh` runs the dictionary `blockMeshDict` located in the `constant/polyMesh`-directory. In `blockMeshDict` nodes and vertices are defined using a right handed coordinate system. Meshing through `blockMeshDict` is text-based and requires some practice. Running the `checkMesh`-utility adds more control to the user in a way that it allows to check the quality of the mesh during pre-processing. The output from this utility is number of cells, max aspect ratio, skewness and non-orthogonality of the mesh to mention a few.

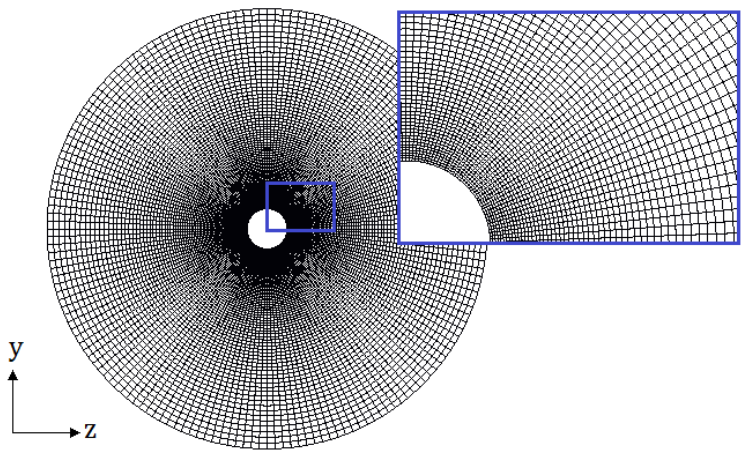

Figure 4.3: Grid topology.

4.1.6 Boundary- and initial conditions

The flow problem is defined in terms of initial- and boundary conditions; it is a required part of the mathematical model. Boundary condition constitutes physical boundaries such as walls, inlets and outlets. At the boundaries certain conditions are prescribed to velocity and pressure, as well as for the turbulence variables. It is important that these are specified correctly so that they do not affect the flow in an unphysical manner. Initial conditions define known field values prior to the first time step. While boundary conditions are set for the whole simulation, initial conditions have a more transient effect as they will converge during simulation. The cylinder is placed in a cylindrical domain, as illustrated in Figure 4.4. The free-stream is bounded by four boundaries; the cylinder wall, inlet, outlet and the far field. The main stream is defined in the x-direction and relevant dimensions are listed in Table 4.1.

The length of the towed array extends over several kilometres. Due to the symmetry of the cylinder it is sufficient to model just a small part and apply cyclic condition to the inlet and outlet. For cyclic boundary conditions the flux of the flow variables at the outlet equals the flux entering the inlet. In this way, the length of the cylinder is only limited by the end-time of the simulation. For external flows the far field is an artificial boundary defined to restrict the flow to a certain volume. The location of this should be set at a reasonable distance so that it does not affect the flow close to the cylinder. To allow the flow to "leave" the computational domain without being reflected by the far field, the gradient of the flow parameters is set equal to zero.

The interaction between the fluid and the cylinder surface will give rise to the no-slip condition due to viscous effects. The velocity at the cylinder surface is therefore set equal to zero; $\vec{V} = [0, 0, 0]$. The eddy viscosity ν_t and the effective viscosity $\tilde{\nu}$ is also affected by the presence of the cylinder. Close to the surface, turbulent viscosity is negligible and they can be set to $\nu_t = \tilde{\nu} = 0$. In the direction normal to the cylinder surface, the pressure-gradient is approximated equal to zero; $\partial p/\partial n = 0$. Two main cases are investigated; a cylinder with and without rotation. For the case of rotation the cylinder surface is assigned a specific rotational speed. The free stream region is the area where the flow is not affected by the boundaries. Here, the initial values of the flow quantities should be specified.

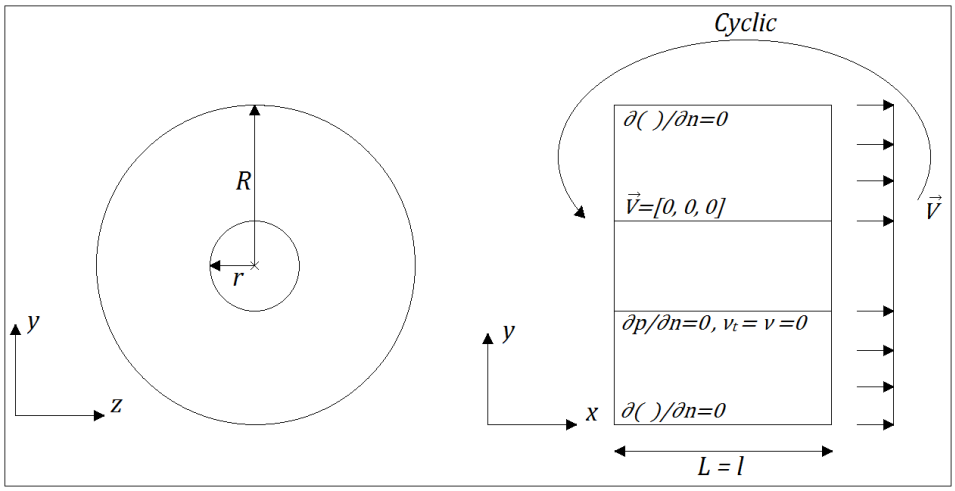

Figure 4.4: Schematic sketch of the flow problem.

Table 4.1: Dimensions of cylinder and computational domain.

Cylinder	$r = 1/11\ m$	$l = 0.5\ m$
Domain	$R = 1.0\ m$	$L = 0.5\ m$

4.2 The OpenFOAM solver pimpleFoam

Two issues arise when we consider the momentum and continuity equation ((3.5)-(3.8)) Firstly, the convective terms in the momentum equations are non-linear. Secondly, all equations are coupled since the velocity appears in both the continuity- and momentum equation. The pressure is defined in the momentum equation for all directions, but there are no equations to solve this explicitly. These problems can be tackled by use of iterative solution strategies. In this thesis the pressure-velocity coupling in the discrete Navier-Stokes equations is solved using the PIMPLE algorithm, a combination of the SIMPLE and PISO algorithm [50]. The corresponding solver in OpenFOAM is called `pimpleFoam`, a transient solver for incompressible flow and is designed to handle large time-steps. SIMPLE is an acronym and stands for Semi-Implicit Method for Pressure Linked Equations. It was formulated by Patankar & Spalding [51] and is the core algorithm for most numerical codes. In a simplified manner the procedure can be explained as follows:

1. An initial pressure field p^* is guessed, or taken from the previous time-step, to obtain the velocity field V^* from the momentum equation. This is referred to as the predictor step.
2. The velocity will not satisfy continuity unless the pressure is corrected. A correction of the pressure p' is introduced so that the total pressure becomes $p = p^* + p'$. This is called the corrector step.
3. A new velocity field is calculated from p to satisfy continuity.
4. Step 1-3 is repeated until convergence is achieved.

In step 2 a correction to the pressure p' is introduced, however when p^* is far from the correct solution divergence may occur during iteration of the equations. To overcome this a relaxation-factor is added to the correction; $p^{new} = p^* + \alpha p'$. When α is equal to 1 the pressure field is corrected by p', and a value of α equal to zero corresponds to no correction. The relaxation-factor is useful to speed up or slow down the changes in the iterative process. An over-relaxation is applied if it is desirable to speed up the process, and an under-relaxation is applied to slow it down. Under-relaxation corresponds to $0 < \alpha < 1$ and is more commonly used. It is noted that the use of relaxation factors are not applicable for transient flow problems. The PISO (Pressure Implicit with Splitting of Operator) algorithm may be regarded as an extension of SIMPLE and was first proposed by Issa [52] for finite difference schemes. A finite volume formulation was presented by Jasak [53] and the procedure is described as follows:

1. An initial value of the pressure field p^* is guessed to obtain the velocity field V^* from the momentum equation. This is called the predictor step.
2. The velocity field V^* will not satisfy continuity unless the pressure is corrected. The new pressure is written $p^{**} = p^* + p'$, where p' is the correction. A new velocity field V^{**} is calculated. This is called the first corrector step.
3. A second correction of the pressure and velocity field is conducted using p^{**} and V^{**}. This is called the second corrector step.
4. Step 2-3 can be repeated a number of times, and this repetition is referred to as PISO-loops.

In the PIMPLE algorithm the whole iteration procedure is repeated a specified number of times, referred to as PIMPLE-loops. If the number of PIMPLE-loops equal to one the algorithm reduces to PISO. In OpenFOAM the number of PISO-loops are controlled by `nCorrectors` and the PIMPLE-loops is controlled by `nOuterCorrectors`. The number of loops affects both computational time and accuracy of the solution. The more loops the greater the computational cost, on the other hand the achieved accuracy is not necessary equivalent high.

4.2.1 Linear solver control

When the Navier-Stokes equations are linearized they take the form $\boldsymbol{Ax} = \boldsymbol{b}$, where $\boldsymbol{A}$ and $\boldsymbol{b}$ are matrices. The linear solver control controls how this equation system is solved. Two linear solvers are used in this thesis; the *preconditioned conjugate gradient* (PCG) and the *preconditioned bi-conjugate gradient* (PBiCG), which are standard solvers.

Without going into much detail, a conjugate gradient is a method of solving symmetric and positive-definite matrices. The principle behind the conjugate gradient is to start with an initial guess of the solution and gradually improve the answer through the iteration procedure. For each step a residual r is calculated, $r = \boldsymbol{b} - \boldsymbol{A}x$, which becomes smaller and smaller for each step. Preconditioning is a technique used for improving the conjugate method and solves the system $\boldsymbol{C}^{-1}\boldsymbol{A}x = \boldsymbol{C}^{-1}\boldsymbol{b}$, where $\boldsymbol{C}$ being the preconditioner [54]. Explained in simple terms, the preconditioner improves the propagation of information through the cells.

There are several options when it comes to the preconditioner $\boldsymbol{C}$. For the present case the *diagonal incomplete-Cholesky* (DIC) and *diagonal incomplete-LU* (DILU) preconditioners are chosen. The PCG and DIC is applied to the pressure, and PBiCG and DILU is chosen for the velocity and turbulence properties. A more thorough explanation of the preconditioned conjugate gradient algorithm is given by Caraba [55].

4.2.2 Stability of numerical solution

To ensure temporal accuracy and numerical stability the Courant-Frederich-Levy condition has to be considered. This condition can be expressed in terms of a coefficient, the CFL number, and acts as a limit for how far the fluid can travel during one single time-step. If the fluid is allowed to travel too far the results may diverge or become erroneous. The CFL number has the following form:

$$CFL = \frac{\Delta t|V|}{\Delta x} \tag{4.8}$$

where Δt is the time-step, $|V|$ is the magnitude of the velocity through a cell and Δx is the size of the smallest cell. In order to maintain stability of the solution the CFL number should not exceed a certain value. This value depends on the solver in use. For an explicit solver CFL should be < 1, and for implicit solvers the value may be larger. Because the magnitude of $|V|$ and Δx vary during run-time Δt should be adjusted to meet the requirement. The `pimpleFoam` solver is semi-implicit because it apply the Euler backward method in time with explicit corrections to account for non-orthogonality in the mesh and non-linear terms amongst others, hence the CFL number should be kept below 1.

5 Convergence study

Before any measurements can be discussed or compared the quality and reliability of the solution has to be ensured. The quality of the solution is affected by the number and size of the cells, as well as their distribution in the computational domain. Few cells may cause poor results because important flow characteristics are not captured. If the computational domain is too small, blockage effects may occur. That is, the area of interest is affected by the far field boundaries resulting in a less reliable solution. Another factor that has to be considered is the computational time. Computational time means the time it takes to perform a numerical simulation and is highly affected by the size of the domain and number of cells. Convergence studies are performed to ensure solution quality and to find an optimal combination of the abovementioned factors. This type of analysis is comprehensive, and probably the most time-consuming activity when performing numerical calculations. The aim is to find a good compromise between accuracy and computational cost.

This chapter summarizes the findings from a parameter- and mesh independency study. The influences of equation solver tolerance, PIMPLE- and PISO-loops are also investigated. Preliminary simulations are performed for a cylinder without rotation. The resultant monitoring parameters are the frictional drag coefficient and wall shear stress at the cylinder surface. Details of simulation set-up are found in Appendix A.

5.1 The frictional drag and wall shear stress

For engineering application the drag coefficient is one of the most important parameters. The non-dimensional coefficient is used in the estimation of the total resistance on a body. It is commonly divided into frictional drag and form drag, where frictional drag is due to viscous interaction with the body and fluid, and form drag originates from the effect of shape. For bodies experiences lift, such as airfoils, an induced drag is included. In this case, the frictional drag is calculated as:

$$C_{df} = \frac{F_f}{A_{ref} \cdot 0.5 \cdot \rho \cdot V_\infty^2} \qquad \textbf{(5.1)}$$

where F_f is viscous force, A_{ref} is projected cross sectional area of the cylinder and V_∞^2 is free stream velocity at the inlet. F_f is calculated by integrating the skin-friction force over the cylinder. Wall shear stress is defined as the tangential force per unit area exerted by the fluid flow and is proportional to the velocity gradient normal to the wall [56]. In OpenFOAM it is calculated as:

$$\tau_w = \nu_{eff} \frac{\partial \vec{V}}{\partial n} = (\nu + \nu_t) \frac{\partial \vec{V}}{\partial n} \tag{5.2}$$

where ν_{eff} is called the effective kinematic viscosity and is the sum of the kinematic- and turbulent viscosity, ν and ν_t respectively. $\partial \vec{V} / \partial n$ is the velocity gradient normal to the cylinder surface. Equation (5.2) implies that the velocity gradient is a linear function of the wall shear stress.

5.2 Convergence of friction drag

Ensuring convergence of statistics to a steady value is the first thing one has to consider. As long as the flow quantities changes with time the solution has not converged. In a converged solution the results will not change significantly when the simulation is run for additional time-steps. A non-zero change with time is not the aim of the test, but when the changes are small and/or periodic it is said to have reached a steady value. In the preliminary tests a uniform distribution of the initial condition is applied.

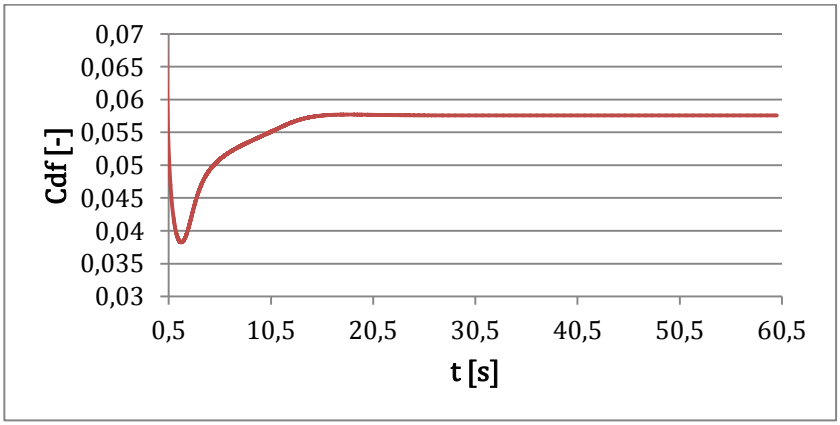

Figure 5.1: Development of C_{df} during simulation.

Figure 5.1 indicate how the frictional drag at the cylinder surface develops over time. Relative large values occur the first 0,5 seconds due to unphysical initial conditions. These are omitted. Because the problem is time-dependent, the distribution of initial values is not important since the flow evolves and will eventually take the correct form. Around $t = 34\ s$ the changes in C_{df} is in the order of 10^{-6}. These are so small that they are considered insignificant and we may say that a steady value is reached. The time-rate-of-change of any parameter is proportional to the residual in the iterative Navier-Stokes equations and for this reason convergence is not reached while this is non-zero. Using the residual as a convergence indicator is therefor also helpful.

Utilizing only the frictional drag coefficient as a measure of convergence has its limitations; firstly, there may be other quantities converging slower than C_{df}. If these quantities are significant for the solution of the investigated case, the results will obviously be questionable. Secondly, spurious results may occur. Using more than one monitoring parameter may be helpful in a way to identify the overall trend in the convergent solution. For example the pressure coefficient C_p could be used as an additional monitoring parameter.

To check the stability of the solution the CFL number has been plotted with respect to time (Figure 5.2). The number stabilizes after about 17 s where it becomes constant. Even though the number is above the recommended limit of 1, the fact that it remains constant indicates a good stability of the numerical results.

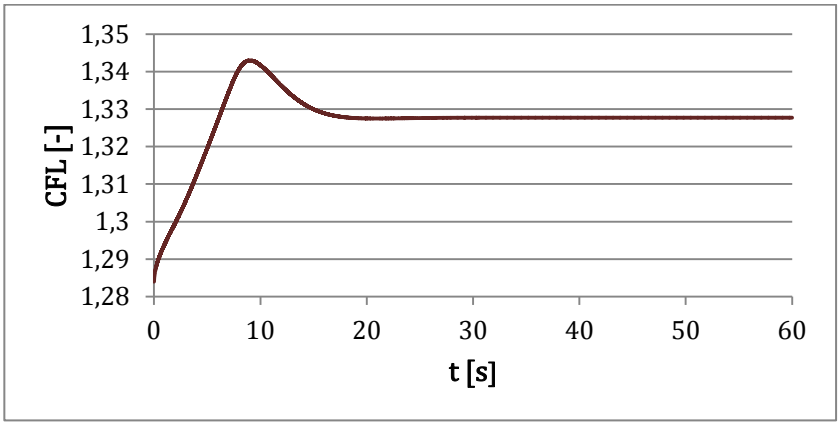

Figure 5.2: Development of CFL number during simulation.

5.3 Mesh independency study

The second type of convergence investigated is mesh independency. The principle of mesh independence study is to start out with a simulation that meet the criteria of convergence and gradually increase the number of cells in the computational domain. When the solution does not change with increasing number of cells it is independent of the mesh. Complete mesh independence will in most cases lead to such a high number of cells that the achieved accuracy is not justified by the increased computational cost. More preferably, the relative error with respect to the finest mesh is calculated to evaluate the quality of coarser mesh.

The solution is also limited by the validity of the turbulence models and their corresponding wall functions. The validity is usually measured by means of the shear velocity based Reynolds number Re_τ and the non-dimensional parameter y^+. An uncritical increase of cells should then be avoided. In the case of applying the S-A model, no wall functions are necessary as the model assumes the first grid point to be in the linear sublayer. Six different cases are tested and the number of cells in each mesh is indicated in Table 5.1 . In this study, attention is paid to the region close to the cylinder as the value of y^+ is important for resolving the boundary layer.

Table 5.1: Number of cells in x-, r- and θ-direction in computational domain.

Mesh	x-direction	r-direction	θ-direction
Mesh_1	60	40	80
Mesh_2	60	50	100
Mesh_3	60	70	140
Mesh_4	60	90	180
Mesh_5	60	110	220
Mesh_6 (reference)	60	130	260

y^+ is calculated at a single point along the cylinder surface for each mesh according to equation (3.1) and the result is shown in Table 5.2. Because y^+ depends on the wall shear stress it will not be constant over the cylinder surface, but it is assumed that they are in the range of the presented values. As the linear sublayer is defined in the range of $0 < y^+ < 5$, clearly, all regions of the turbulent boundary layer is captured for all the mesh types.

Table 5.2: Calculated y^+ for the different meshes in the mesh independency study. Values extracted from $x = 0.25\ m$.

Mesh	y^+ $[-]$
Mesh_1	3.55
Mesh_2	2.83
Mesh_3	2.02
Mesh_4	1.57
Mesh_5	1.28
Mesh_6 (reference)	1.09

Figure 5.3 shows the frictional drag coefficient and wall shear stress at the cylinder surface plotted with respect to increased number of cells in the domain. The reference mesh (*Mesh_6*) is also included here. It is observed that the slope of C_{df} and τ_w decreases with increasing number of cells in the domain because the results are approaching the reference value. The error is therefore decreasing. The computational time increased with nearly 600% from the coarsest mesh to the finest. A trade-off between the achieved accuracy and computational cost is then needed.

Generally, the deviations are small with a maximum error of 1.92% for C_{df} and 1.95% for τ_w. Errors below 1% are treated as acceptable; hence the four last meshes (including *Mesh_6*) are usable. Even though the finest mesh is expected to be well-resolved, limitations due to extensive computational time make it difficult to use it for further investigations. Figure 5.3 show that complete mesh independency is not accomplished. If one was to achieve this the number of cells had to be further increased beyond the reference mesh. Most likely the deviations are smaller than those presented here, so further increase is unnecessary. *Mesh_3*, with $972\ 000$ cells, is chosen as acceptable and is used in the remaining calculations. This decision was made on the basis of the achieved y^+-value, accuracy and time required to finish the run.

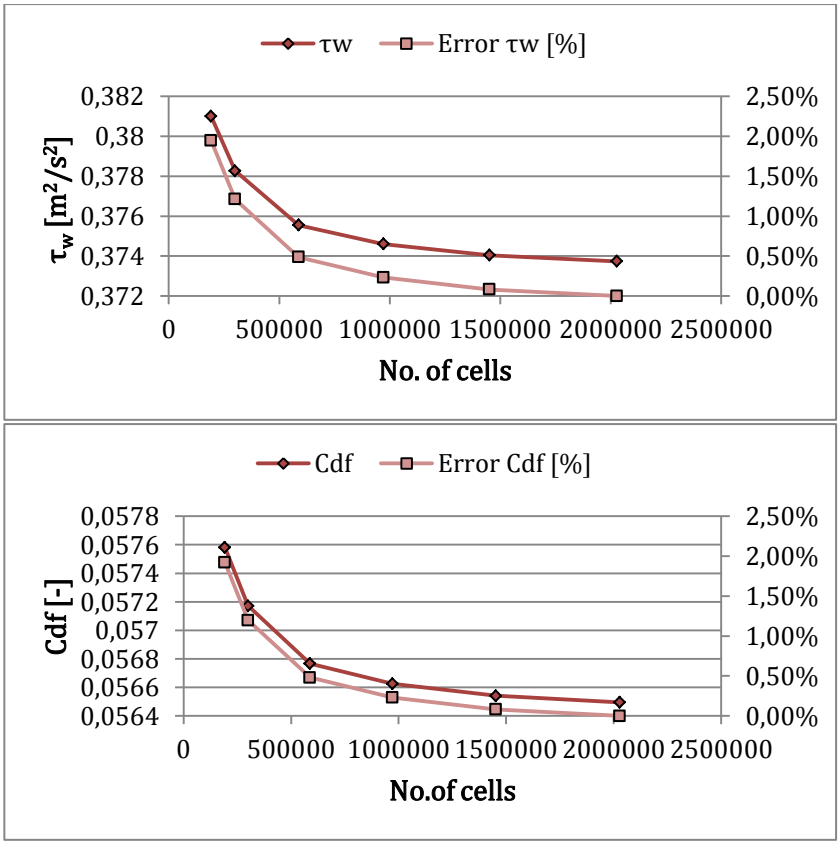

Figure 5.3: Effect of increased number of cells. Values extracted from $x = 0.25\ m$.

5.4 Number of PIMPLE- and PISO-loops

The PIMPLE algorithm relies on evaluating a guessed solution. For how many times the solution should be corrected is determined by the number of loops, and in OpenFOAM the user is free to specify any combination of the PIMPLE- and PISO-loops. Usually not more than 4 loops are required for each of the two.

The aim of increased number of PIMPLE-loops is to gain higher accuracy. Having said, increasing the number of PIMPLE-loops has also shown significant increase in computational time. Keeping this number at a minimum while at the same time maintain desired accuracy is beneficial. In this analysis four different numbers of PIMPLE-loops have been tested, ranging from $1 - 4$. Results generally show that an increased number has a negligible effect on the solution (see Figure 5.4). The changes are about $5 \cdot 10^{-5}\%$ whereas the

computational cost increased with over 200% from 1 PIMPLE-loop to 4 PIMPLE-loops.

As for the PIMPLE-loops the aim of increased number of PISO-loops is to achieve higher accuracy. Four different PISO-loops have been tested, ranging from $1-4$ while the number of PIMPLE-loops is set to 1. Again, the relative error between the different PISO-loops is quite small and provides more or less the same answer. The difference is about $5 \cdot 10^{-5}$% from the configuration with 1 PISO-loop to the one with 4 loops. Although Figure 5.5 indicate that a fully converged solution with respect to increased number of PISO-loops is not achieved the deviations are practically zero. Applying more than 1 PIMPLE- and PISO-loop is therefore unnecessary.

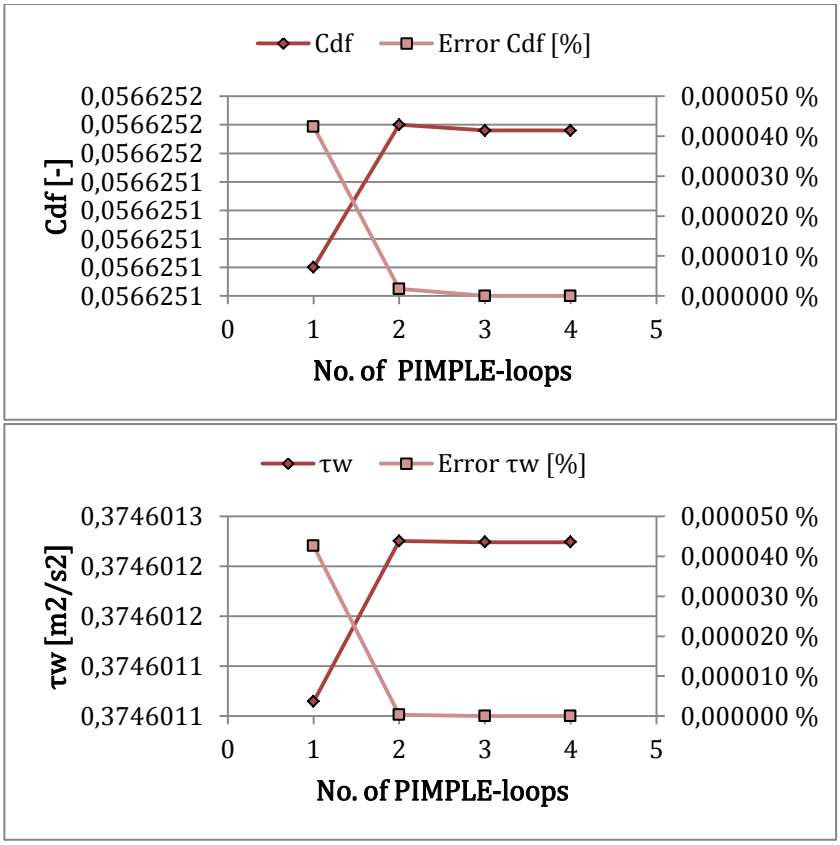

Figure 5.4: Effect of increasing number of PIMPLE-loops. Values extracted from $x = 0.25\ m$.

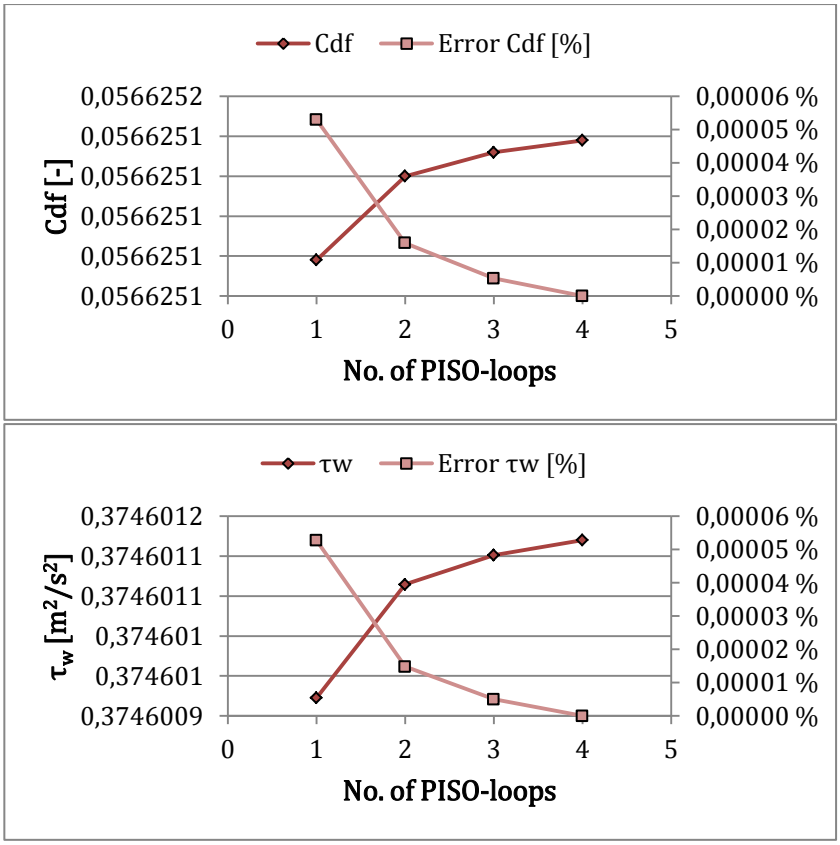

Figure 5.5: Effect of increasing number of PISO-loops. Values extracted from $x = 0.25\ m$.

5.5 Solver tolerance sensitivity

Solving the linear equation system by iterative technique is based on reducing the residual that arises from guessing an initial solution. It is evaluated by substituting the current solution into the equation and taking the magnitude of the difference between the left- and right hand sides [57]. The solver tolerance is set such to reduce the residual. The smaller the residual, the more accurate solution is obtained. When the residual is below a specified tolerance the iteration procedure is terminated.

In OpenFOAM this is defined by the `tolerance`-keyword and is specified for all calculated variables. For the S-A model this include the pressure, velocity and the effective viscosity $\tilde{\nu}$. The velocity and $\tilde{\nu}$ have equal tolerance while the pressure is set one tenth lower. In this convergence study the tolerance is gradually lowered to reveal how the results are affected. The

pressure tolerance was varied from $10^{-5} - 10^{-9}$ and correspondingly the velocity and $\tilde{\nu}$ varied from $10^{-4} - 10^{-8}$.

As expected the number of iterations for the pressure, velocity and $\tilde{\nu}$ increased for decreased tolerance level. When the tolerance becomes tighter the solver has to perform additional iterations to meet the criteria. It is seen (Figure 5.6) that a tighter tolerance have a negligible effect on the solution. The convergence study shows that the results generally are insensitive to the number of PIMPLE- and PISO-loops and decreased tolerance.

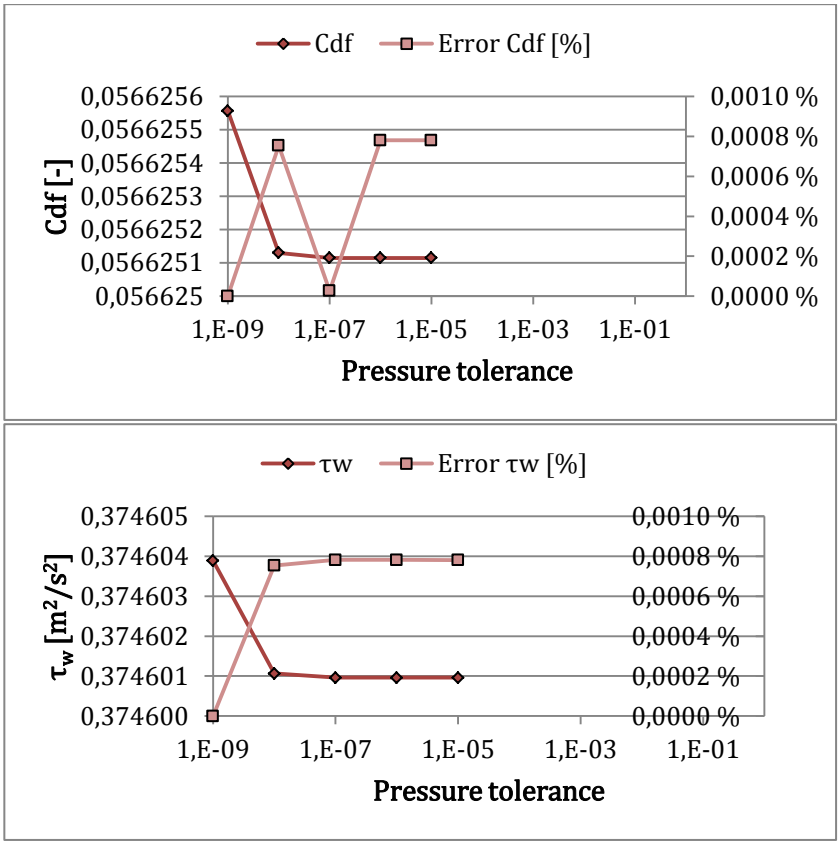

Figure 5.6: Effect of tolerance level.

6 Results and discussion

In this section results from simulations of flow along a cylinder with and without rotation is presented. The simulations are carried out for Reynolds number $Re_\tau = [240,\ 550]$ and the ratio of axial to rotational velocities are $U_\theta/U_x = [0,\ 0.5,\ 1.0]$. From the convergence study the influence of several key numerical parameters on accuracy and computational time was investigated. For faster convergence of flow parameters, the flow field from the last time-step of the optimal configuration are mapped into new cases. All simulations are run for 60 time-units.

Results are then used in a comparative study with LES data. While the LES method provides instantaneous values of the flow quantities, the RANS approach give time-averaged statistics. It is therefore necessary to subtract the mean quantities from the instantaneous to obtain time-average data from the LES approach. Important parameters in boundary layer analysis are the plus-units, Reynolds shear stresses and turbulent eddy viscosity.

The advantage of applying the S-A model is that it does not require wall functions, hence, one less thing to take into consideration when assessing the flow set-up. In addition, the transport equation is defined in such a way that the flow will never exhibit laminar structure. Since time-averaged statistics is the output from RANS the characteristic eddies will not be visible in the resulting flow field.

Because the flow is modelled as pressure driven a pressure-gradient has to be imposed. The magnitude of this should correspond to the desired Re_τ. In OpenFOAM, this is done by specifying a bulk velocity. The mean wall shear stress that arises due to the bulk velocity is equivalent to the time-average of the pressure-gradient. The relation between the wall shear stress, shear velocity and pressure-gradient is given by:

$$-\frac{\partial p}{\partial x} = \frac{\tau_w}{H} = \frac{u_\tau^2 \rho}{H} \qquad \textbf{(6.1)}$$

and is achieved by considering the overall momentum equation. For the free stream region the velocity is set equal to the bulk velocity in all cases. Since the pressure-gradient is defined implicitly by Re_τ one cannot know in advance what value to assign the bulk velocity. An iterative approach is needed to solve this; the bulk velocity is guessed and Re_τ is calculated from the converged solution. This procedure is repeated until the Reynolds number reaches the desired value of 550 and 240. However, one must also take into account the y^+-parameter

because the velocity also affects the value of this. First, results from a stationary cylinder will be presented followed by a cylinder of rotation.

6.1 Cylinder without rotational velocity

The Reynolds shear stress $-\overline{uv}$ is calculated based on the velocity gradient normal to the cylinder surface:

$$-\overline{uv} = 2 \cdot \nu_t \frac{\partial U_x}{\partial n} \tag{6.2}$$

Below are presented the data from the RANS- and LES approach for a cylinder without rotation. The data is taken from the last time-step of the converged solution. In the free-stream region a bulk velocity of $10.70\ m/s$ and $4.3\ m/s$ corresponded to $Re_\tau = [240,\ 550]$ respectively. The kinematic viscosity was set to $\nu = 1 \cdot 10^{-3}\ m^2 s^{-1}$, while the effective- and eddy viscosity was assigned the values $\tilde{\nu} = \nu_t = 10 \cdot \nu$.

For boundary layer type of flows the Reynolds shear stress $-\overline{uv}$ is the most important parameter affecting the mean motion as it controls most of the momentum transfer. $-\overline{uv}$ is also directly related to the frictional drag at the wall surface. Figure 6.1 display the resulting $-\overline{uv}$ from RANS and LES. Also included is the distribution of viscous shear stress. Several distinct regions are identified in the plot. In the region closest to the surface the viscous shear stresses are dominant whereas the Reynolds shear stresses are zero. This region is recognized as the viscous sublayer, or the linear sublayer. Because the eddy viscosity is zero at the surface (according to no-slip condition) $-\overline{uv}$ is also zero. It is therefore approximated that the shear stresses in this region are only a result of viscous action. This means that the relevant parameters are the shear velocity u_τ and the kinematic viscosity ν. The assertion of linearity comes from a linear variation of the velocity in this region. Moving further away from the viscous sublayer the Reynolds shear stresses peaks (about $y^+ = 25$), this occurs in the buffer layer where most of the turbulent energy production and dissipation takes place. Here, both $-\overline{uv}$ and viscous shear stresses are of equal importance.

After $-\overline{uv}$ peaks the viscous shear stresses drops to an almost constant value. This region is called the constant stress-layer. Here, Reynolds shear stresses are substantial meaning that the momentum transfer is more or less due to turbulence. In dimensional form the total shear stresses are approximate to the wall shear stress τ_w. Table 6.1, where τ_w and peak value of $-\overline{uv}$ is given, confirms this to some extent. Using the term constant stress layer is somewhat inaccurate in the case of low Reynolds number because the constant region is non-existing. For increased Reynolds number the peak will generally increase, move away from the wall and gradually flatten. This effect is not seen in Figure

6.1 due to the range in Reynolds number is too small, but is better illustrated in the article by Sreenivasan [58] (Fig. 4). As a part of a turbulent skin friction study Monte et. al. [59] investigated the influence of Re_a (Reynolds number based on cylinder radius) and Re_δ (Reynolds number based on boundary layer thickness) on the Reynolds shear stresses. With varying Re_a and constant Re_δ the peak value of $-\overline{uv}$ moved away from the wall and increased with increasing Re_a. The localization of the shear stress peak did not vary for increasing Re_δ (and constant Re_a), but became wider while decreasing in value. This means that the Reynolds shear stresses become important for a larger part of the log-layer and that the turbulent contribution decreases for increasing boundary layer thickness. The distribution of $-\overline{uv}$ is similar for both the RANS and LES approach.

Vorticity describes the local rotational motion of the fluid which is, in mathematical form, expressed as the curl of the velocity vector:

$$\vec{S} = \nabla \times \vec{V} \qquad \textbf{(6.3)}$$

The unit of the vorticity is s^{-1} and the calculated magnitude is shown in Figure 6.2 Even though the surface is not the source of the vorticity it is concentrated in this region. Calculations show that the bulk of vorticity takes place in the normal direction of the cylinder and are diffused outwards. The components can also be estimated by considering the velocity distribution because it is directly linked to the velocity vector. In turbulent flows the vorticity intensity is increased with decreasing scales of motion. This is correlated with the energy cascade in which large eddies spawn smaller and smaller eddies. At the smallest scales eddies lose directional preference and are considered anisotropic.

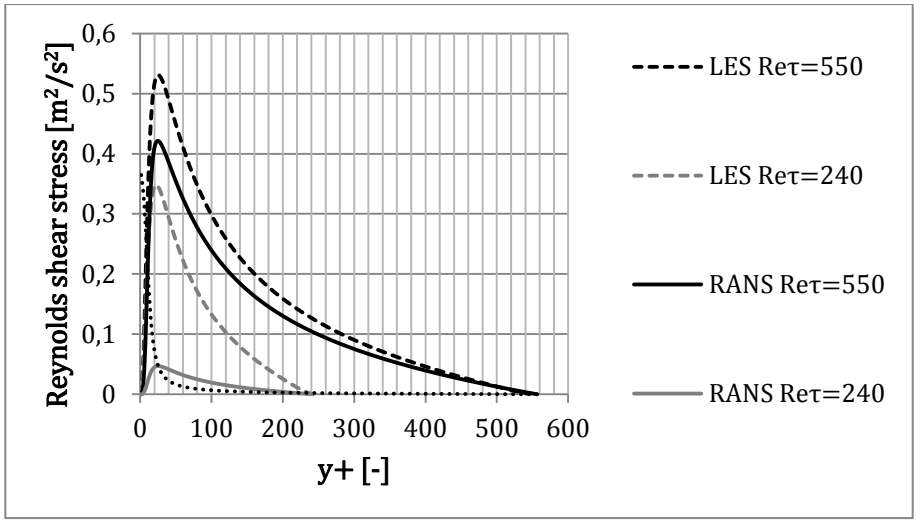

Figure 6.1: Reynolds shear stresses $-\overline{uv}$ from RANS simulation and LES for $Re_\tau = [240,\ 550]$. Values extracted from $x = 0.25\ m$.

Table 6.1: Wall shear stress and peak value of Reynolds shear stress.

	$\lvert\tau_w\rvert\ [m^2/s^2]$	$-\overline{uv}_{peak}\ [m^2/s^2]$
$Re_\tau = 550$	0.374	0.421
$Re_\tau = 240$	0.070	0.046

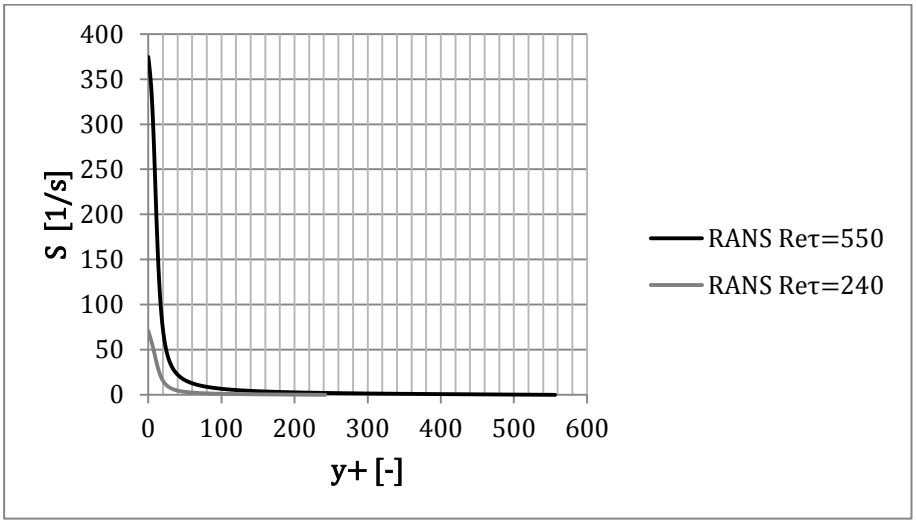

Figure 6.2: Resulting magnitude of vorticity from RANS simulations. Values extracted from $x = 0.25\ m$.

In Figure 6.3 the normalized velocity profile for the axial velocity component U_x^+ is displayed. Dotted lines indicate the law-of-the-wall. Included are the results from RANS and LES for the two Reynolds numbers. The RANS data holds similarities with the classical law-of-the-wall, although it deviates slightly for $y^+ > 100$. The laminar sublayer and buffer layer are clearly visible in the range of $0 < y^+ < 20$. This is in accordance with the findings by Willmarth et. al. [10] where regions in which the two-dimensional law-of-the-wall are seen. While law-of-the-wake is visible in the results of Harun [36], this is not the case here. The results are in fair agreement with the LES predictions and differ only slightly in the log-layer where the S-A model over predicts the velocity. For a flow exposed to a constant adverse pressure-gradient Harun found that an increase of Reynolds number corresponded to a constant shift-down in the profile provided that the Reynolds number range is sufficient large. Having also studied the effect of varying pressure-gradient with constant Reynolds number he suggested that deviations from the log-law were caused by the pressure-gradient. For the present case, both the pressure-gradient and the Reynolds number range are too small to identify any shift-down in the profile. Because of symmetry about the axis the flow field reduces to a two-dimensional problem, i.e. the condition is axisymmetric. In Figure 6.4 the distribution of the axial velocity component in the fluid domain is visualized. The no-slip condition causes U_x to gradually decrease from its free-stream value to 0 at the surface. The distribution of U_x in the domain indicate the two-dimensional behaviour of the velocity; constant in x-direction and varying in the yz-plane. The magnitude of the radial- and circumferential velocities, U_r and U_θ, are zero in this case, indicating that cross-flow effects are absent.

The maximum transported viscosity for S-A occurs for y^+ values larger than 100. Figure 6.5 show the turbulent eddy viscosity distribution across the domain. The distribution of the effective viscosity show similar behaviour as the eddy viscosity. However, the values are quite low. What is expected is ratios in the order of 1000, and the low values in the present case indicate laminar behaviour. Generally, it is advised to use $\tilde{\nu} = \nu/10$ [60], $\tilde{\nu}/\nu = 3$ [43], or $\tilde{\nu}/\nu = 3 - 5$ [61]. Simple tests where the value of $\tilde{\nu}$ and ν_t was varied showed the same trend as in Figure 6.5 with only minor changes in the values of the quantities.

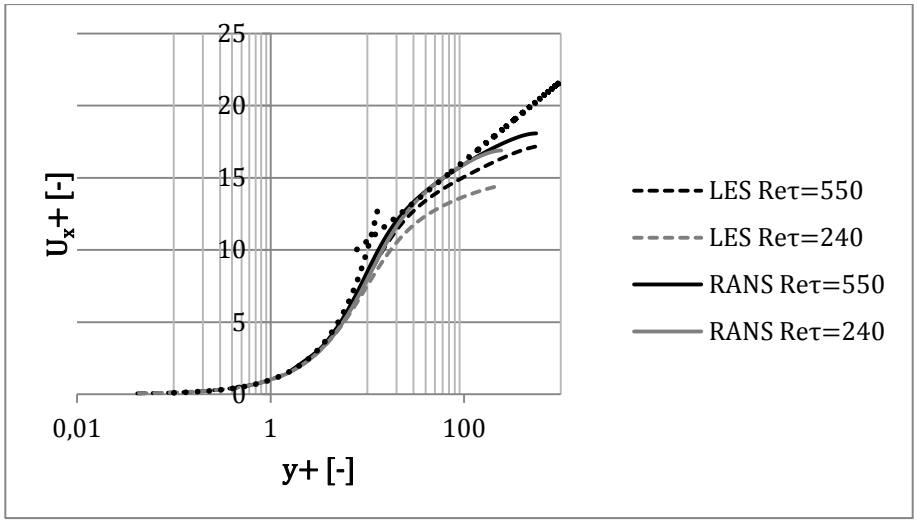

Figure 6.3: Velocity profile from RANS simulation compared to LES for $Re_\tau = [240,\ 550]$. Dotted lines indicate the law-of-the-wall. Values extracted from $x = 0.25\ m$.

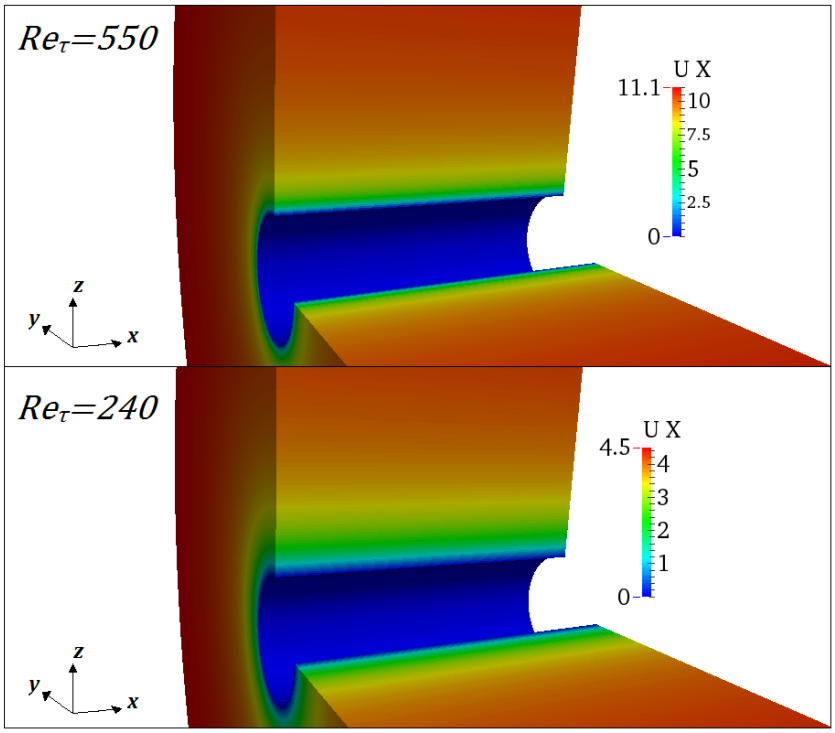

Figure 6.4: Velocity distribution in the axial direction for $Re_\tau = 550$ (upper) and $Re_\tau = 240$ (lower).

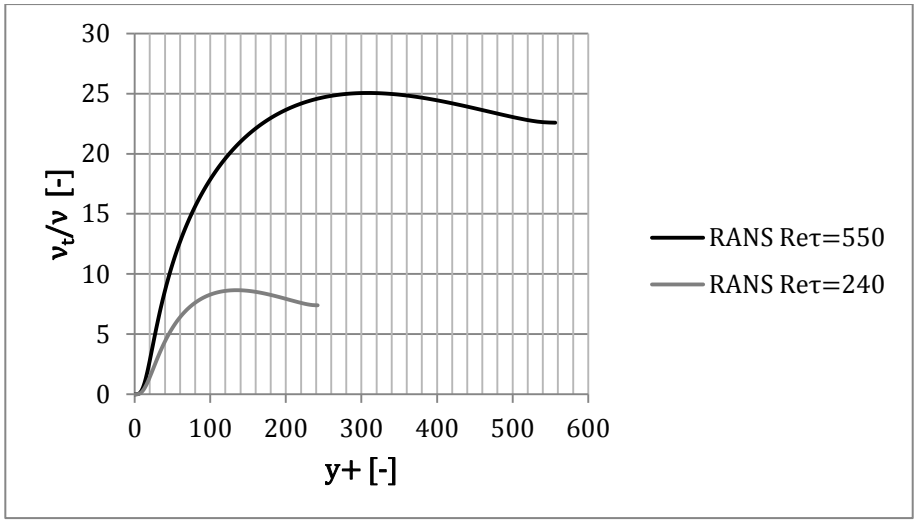

Figure 6.5: Eddy viscosity ratio from RANS for $Re_\tau = [240,\ 550]$. Values extracted from $x = 0.25\ m$.

When the cable is towed through water the greatest pressure will be concentrated in the vicinity of the surface. With increased distance to the wall, the pressure will gradually decrease. This behaviour is very well captured in the LES data in Figure 6.6 (upper). The pressure peaks about $y^+ = 30 - 40$, which is also the case for RANS where $Re_\tau = 240$ (see Figure 6.6 (lower)). Considering the resulting pressure from the RANS approach (where $Re_\tau = 550$), the distribution is unphysical. The fluctuating values do not suggest any concentration of the pressure close to the surface. Figure 6.7 also show how the pressure varies at the cylinder surface for RANS. Because of the fundamental differences between LES and RANS it is not expected that the results will be in the same order of magnitude. It is the general trend in the distribution of the mean quantities that is of interest. Rumsey & Spalart [43] applied the S-A model for different Reynolds numbers and found that the model did not perform well in transition (e.g. low Reynolds number). They concluded that the model was best suited for fully turbulent high Reynolds number computations. Following this, it seems that the S-A model does not perform well in the prediction of pressure in this case.

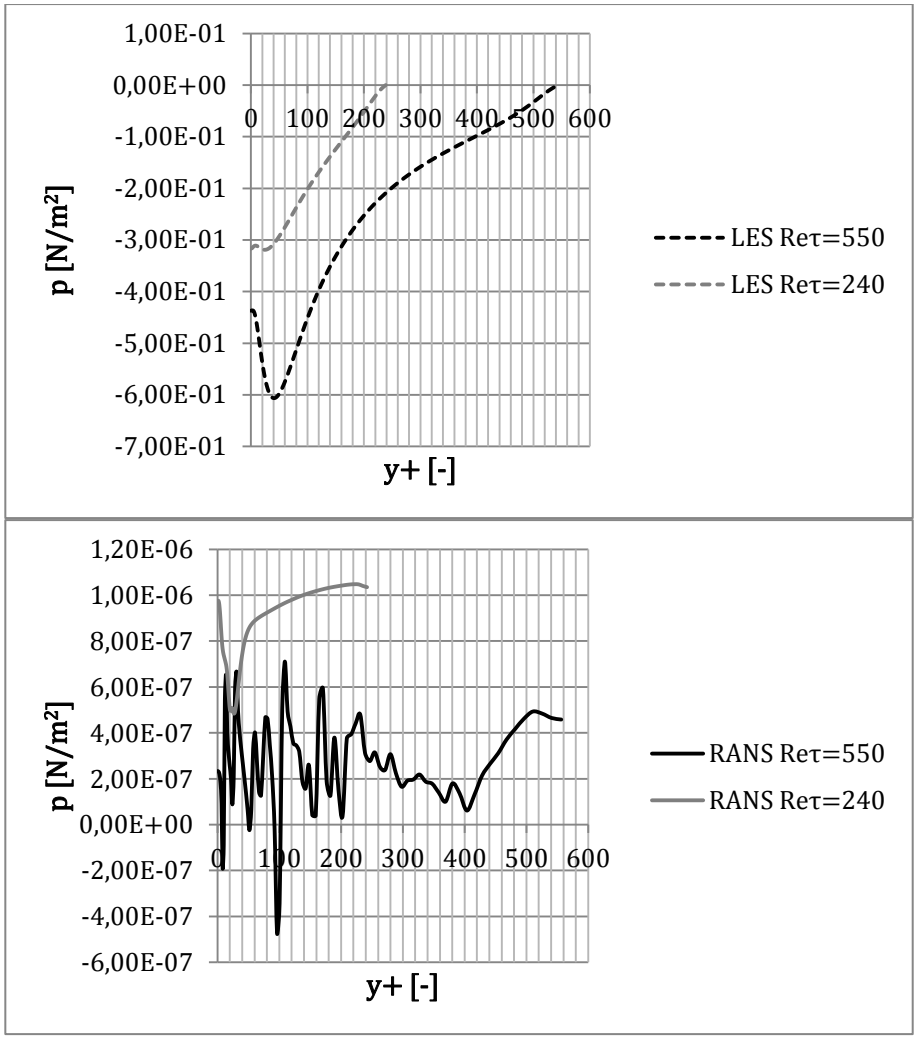

Figure 6.6: Pressure distribution in radial direction for LES (upper) and RANS (lower).

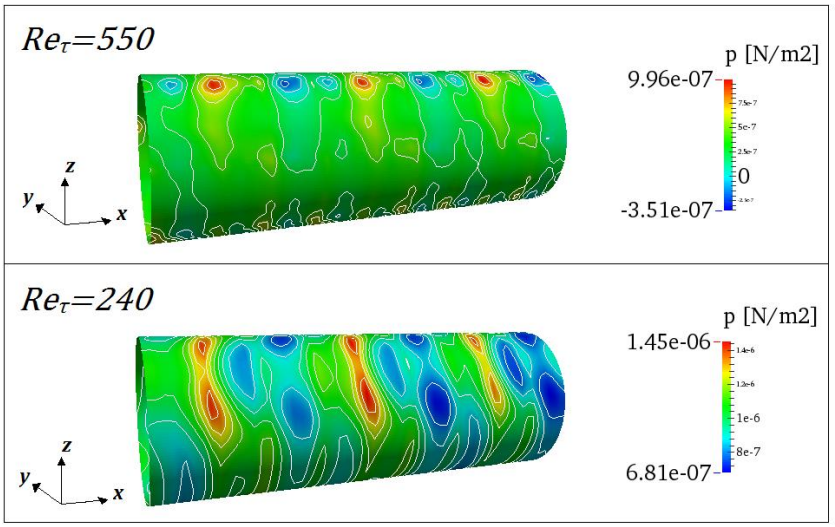

Figure 6.7: Contour plot of pressure distribution from RANS for $Re_\tau = 550$ (upper) and $Re_\tau = 240$ (lower).

6.2 Cylinder with rotational velocity

The analysis in this section is based on results obtained from a cylinder rotating at two different velocities; $U_\theta/U_x = [0.5,\ 1]$. The data is taken from the last time-step of the converged solution. The velocity on a rotating cylinder consists of an axial, radial and circumferential component. This results in a skewed velocity profile because the velocity vector is forced in the direction of rotation at the surface. The adjacent particles are affected by this and propagate outwards in the boundary layer with gradually decreasing strength. The additional velocity components may generate larger velocity gradients and increased turbulence intensity. The frictional drag coefficient is dependent on the rotational-to-free-stream-velocity ratio. This dependency is due to the fluid rotates with the cylinder in the immediate vicinity of the surface where it is subjected to strong centrifugal forces [62].

Figure 6.8 display the normalized velocity profile for the axial velocity component where $U_\theta/U_x = [0.5,\ 1]$. The profiles collapse in the linear sublayer for both RANS and LES. The classical linear sublayer and log-region is indicated by dotted lines. For the LES data there is no identifiable log-region, whereas for RANS it deviates for $y^+ > 100$. Compared to the LES data there are large differences in the profile for the buffer- and log-region (Figure 6.8 upper). Differences within the LES data is observed when comparing the velocity profiles for $U_\theta/U_x = 0$ and $U_\theta/U_x = 0.5$, while the RANS data is more or less unaffected in all the three cases. This is seen by comparing Figure 6.3 and

Figure 6.8. In the previous section it was stated that the velocity components in the radial and circumferential direction was equal to zero. When the cylinder rotates the velocity vector is forced in the direction of rotation causing cross-flows to be significant. This effect is strongest closest to the source of rotation with gradually decreasing strength for increased distance to the cylinder. Plot of the normalized radial velocity component U_r^+ for $U_\theta/U_x = 1$ (Figure 6.9) show the effect of rotation; as y^+ decrease the influence increases.

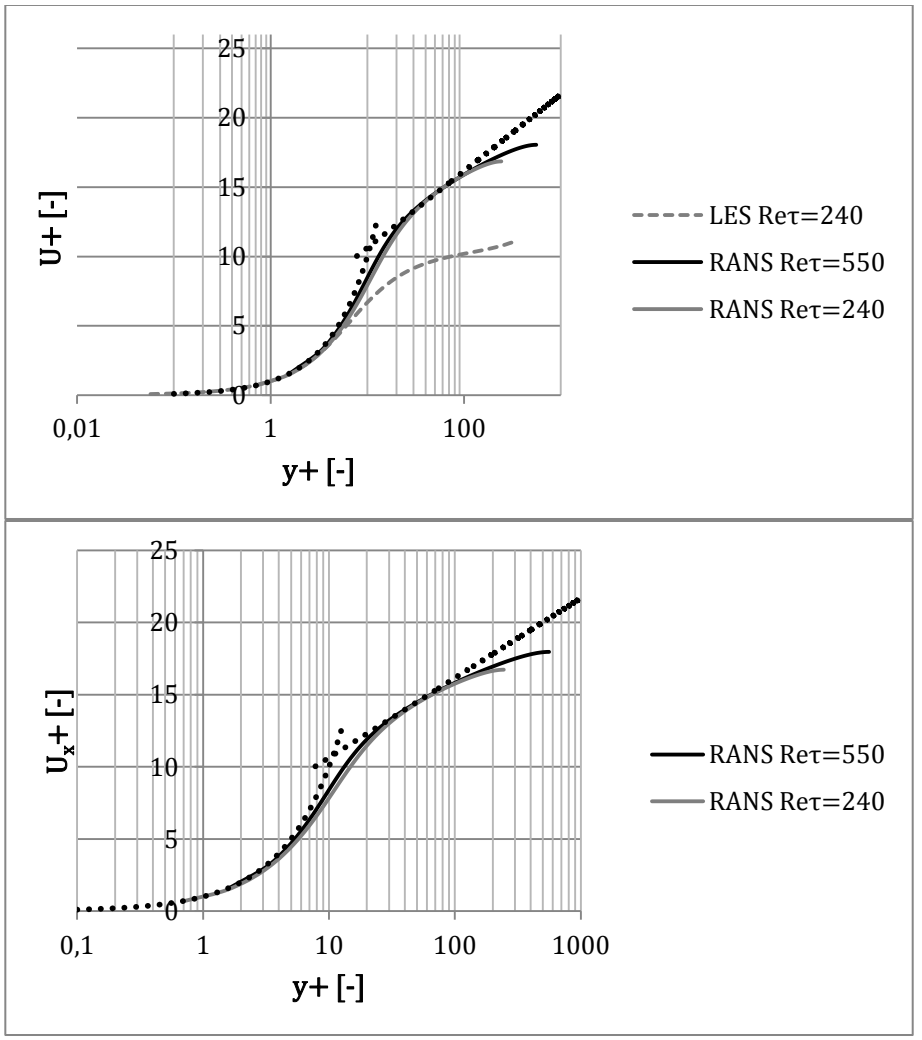

Figure 6.8: Normalized mean velocity profile. Upper; $U_\theta/U_x = 0.5$, lower; $U_\theta/U_x = 1$. Dotted lines indicate the law-of-the-wall. Values extracted from $x = 0.25\ m$.

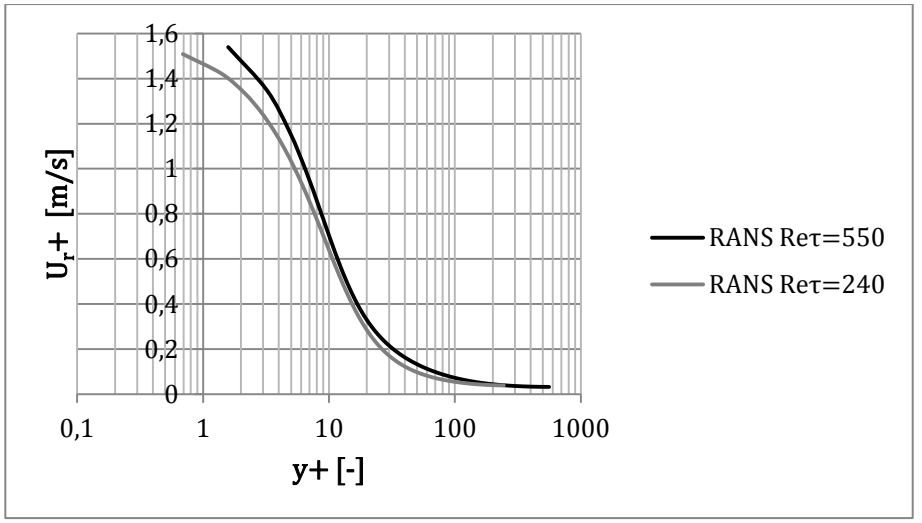

Figure 6.9: Normalized radial velocity component u_r for $U_\theta/U_x = 1$. Values extracted from $x = 0.25\ m$.

Contour plot of pressure at the cylinder surface is displayed in Figure 6.10. As for the velocity, the pressure is also affected by the rotation causing a three-dimensional behaviour at the surface. This is seen by the contour lines varying in all three directions. As mentioned, the greatest pressure is located in the vicinity of the surface with gradually decreasing effect outwards. This is seen Figure 6.11.

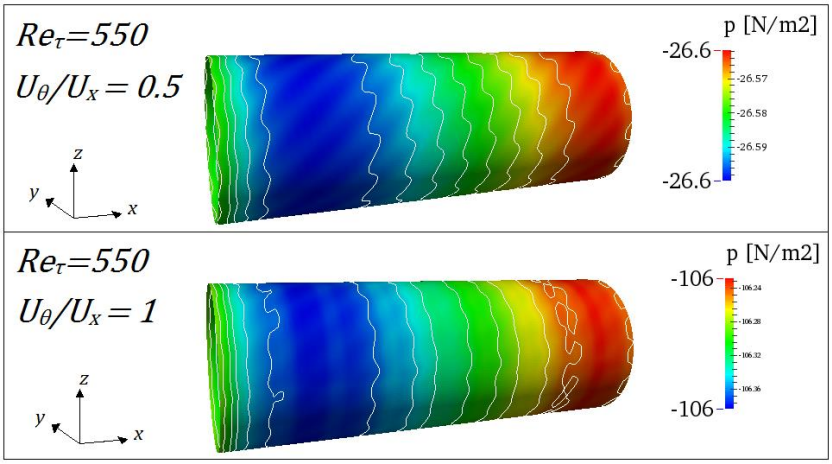

Figure 6.10: Contour plot of pressure at cylinder surface from RANS.

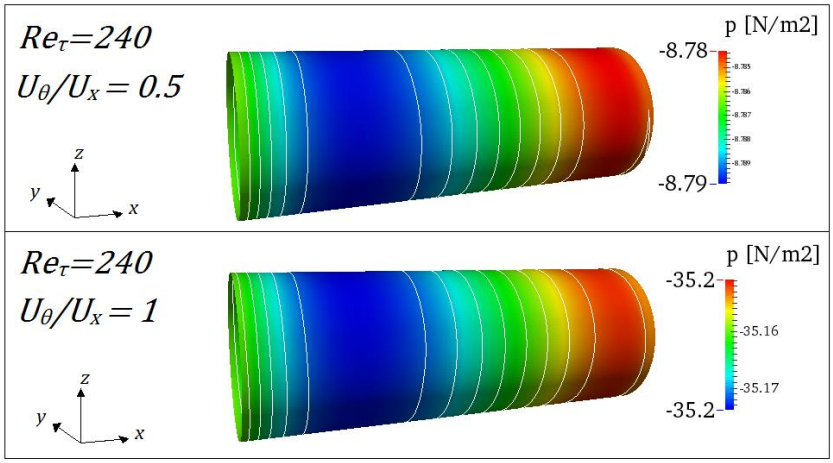

Figure 6.10 continued: Contour plot of pressure at cylinder surface from RANS.

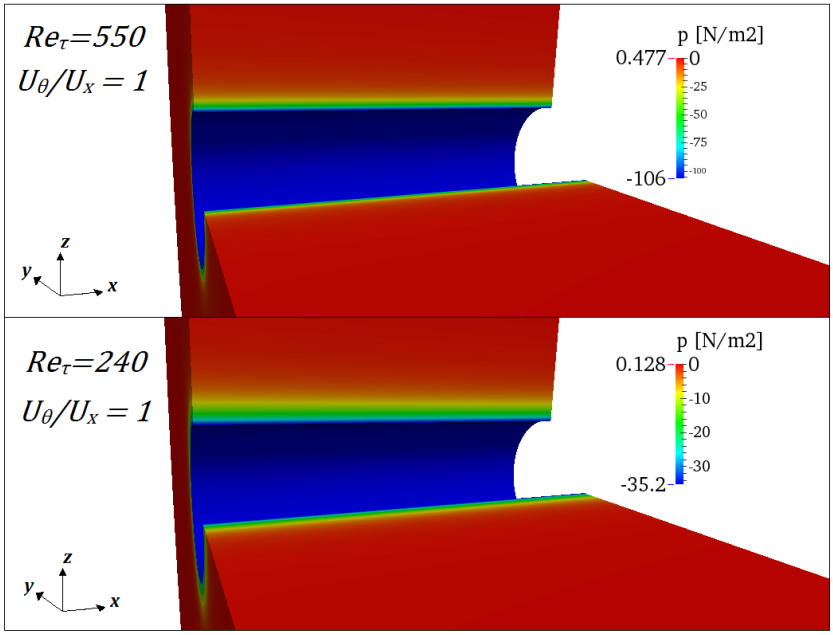

Figure 6.11: Visualization of pressure distribution in fluid domain at $Re_\tau = 550$, $U_\theta/U_x = 1$ (upper) and $Re_\tau = 240$, $U_\theta/U_x = 1$ (lower).

7 Conclusion and recommendations

Numerical calculations of a pressure driven flow along a cylinder are performed for the purpose of investigating the turbulent boundary layer. A convergence study is conducted to ensure the quality of the solution, where special attention is paid to the near-wall region in order to capture all levels of the turbulent boundary layer. Influence on key numerical parameters was investigated in terms of solver tolerance, number of PIMPLE- and PISO-loops, number of cells in the computational domain and time. It was found that that 972 000 cells were sufficient to capture all regions of the boundary layer and that the effect of decreased tolerance and increased number of PIMPLE- and PISO-loops was negligible. In order to make the convergence study more reliable it is recommended to include additional key parameters. Investigating the effect of far field boundary size is also beneficial to avoid possible blockage effects.

The Reynolds Average Navier-Stokes (RANS) approach is utilized in order to solve the flow field, and the Spalart-Allmaras model is used in the prediction of turbulence. Two rotational velocities are applied to the cylinder, in addition to a case of zero rotation, to simulate the behaviour of an acoustic array towed through water. Simulations are carried out for two different Reynolds number based on the shear velocity; $Re_\tau = [240, 550]$ and the velocities are given in terms of the axial velocity component; $U_\theta/U_x = [0,\ 0.5,\ 1.0]$. Because of symmetry about the axis the flow field reduces to a two-dimensional problem in the case of $U_\theta/U_x = 0$. With rotation added cross-flow effects become significant because of centrifugal forces.

Results show that the normalized mean velocity profile is in good agreement with the findings by Willmarth et. al. [10] where regions in which the two-dimensional law-of-the-wall are seen. Comparisons with LES data indicate good agreement with the normalized mean velocities and Reynolds shear stresses in the case of a non-rotating cylinder. However, the pressure distribution is not very well predicted for RANS in this case. When rotation is added a more realistic distribution of the pressure is seen, whereas the normalized mean velocity have a considerably deviation from the LES data in the log-region.

In this study, a turbulence model suited for low-Reynolds number calculations is applied. It has shown to predict the normalized mean velocity in a satisfactory way, but it is of interest for further investigation to apply additional turbulence models. The $k-\omega\ SST$ model applies for both high- and low-Re problems combining the classical $k-\omega$ and $k-\varepsilon$ models to predict the turbulent flow field. The $\bar{v}^2-f$ model has shown success in the prediction of near-wall flows at low Reynolds numbers. It resembles the $k-\varepsilon$ model, but

does not make use of wall functions. A velocity scale $\bar{v}^2$ is used in the prediction of the eddy viscosity and a relaxation factor f to model the anisotropic behaviour close to the wall.

8 Bibliography

[1] A. N. Kolmogorov, “The Local Structure of Turbulence in Incompressible Viscous Fluid for Very Large Reynolds number,” Dokl. Akad. Nauk., 1941.

[2] O. Reynolds, “An Experimental Investigation of the Circumstances which Determine whether the Motion of Water shall be Direct or Sinuous, and the Law of Resistance in Parallel Channels.,” Royal Society Phil. Trans., 1883.

[3] P. A. Durbin and B. Pettersson-Reif, Statistical Theory and Modeling for Turbulent Flow, Wiley, 2011.

[4] C. Kopp, “Identification Underwater with Towed Array Sonar,” in *Pacific Maritime Conference*, 2010.

[5] T. Elboth, H. Qaisrani and T. Hertweck, “De-noising Seismic Data in the Time-Frequency Domain,” SEG Technical Program Expanded Abstracts, 2008.

[6] S. Lemon, “Towed-Array History, 1917-2003,” Journal of Oceanic Engineering, 2004.

[7] E. de Villiers, *The Potential of Large Eddy Simulation for the Modeling of Wall Bounded Flows*, Imperial College of Science, Technology and Medicine, 2006.

[8] T.-S. Cham and R. M. Head, “The Turbulent Boundary Layer on a Rotating Cylinder in an Axial Stream,” J. Fluid Mech., Vol. 42, 1970.

[9] R. M. Lueptow, “Turbulent Boundary Layer on a Cylinder in Axial Flow,” NUSC Technical Report 8389, 1988.

[10] W. W. Willmarth, R. E. Winkel, L. K. Sharma and T. J. Bogar, “Axially Symmetric Turbulent Boundary Layers on Cylinders: Mean Velocity Profiles and Wall Pressure Fluctuations,” J. Fluid Mech., 1976.

[11] N. Afzal and R. Narashima, “Axisymmetric Turbulent Boundary Layer Along a Circular Cylinder at Constant Pressure,” J. Fluid Mech., Vol.74, 1976.

[12] O. R. Tutty, “Flow Along a Long Thin Cylinder,” J. Fluid Mech., 2008.

[13] R. A. Marschall, D. L. Stinson, R. E. Pearce, E. Boyer and B. Embry, “The Use of an Innovative Solid Towed Array for Exploring the Antarctic Marine Environment,” Proc. Oceans '93; Engineering in Harmony with Ocean , 1993.

[14] J. R. Potter, E. Delory, S. Constantin and S. Badiu, “The 'thinarray'; a lightweight, ultra-thin (8 mm OD) towed array for use from small vessels of opportunity,” Proc. Intl Symp. on Underwater Technology, 2000.

[15] T. Elboth, B. A. Reif and Ø. Andreassen, “Flow and Swell Noise in Marine Seismic Data,” Geophysics, Vol. 74, 2009.

[16] T. Elboth, C. E. Wasber, A. Helgeland, Ø. Andreassen and B. A. Reif, “Flow Noise Simulation Around a Cylinder,” Norwegian Defence Research Establishment (FFI).

[17] OpenFOAM Foundation, “OpenFOAM User Guide,” OpenCFD Ltd., [Online]. Available: http://www.openfoam.org/docs/user/. [Accessed 01 05 2014].

[18] D. A. Lysenko, I. S. Ertesvåg and K. E. Rian, “Modeling of Turbulent Separated Flows using OpenFOAM,” Computers and Fluids, 2012.

[19] F. White, Viscous Fluid Flow, McGraw Hill, 2006.

[20] T. Cebeci and J. Cousteix, Modelling and Computation of Boundary-Layer Flows, Springer, 2005.

[21] H. Tennekes and J. Lumley, A First Course in Turbulence, Cambridge,

Mass : MIT Press, 1972.

[22] P. Müller, The Equations of Oceanic Motions, Cambridge University Press, 2006.

[23] W. Frei, "Which Turbulence Model Should I Choose for my CFD Application?," COMSOL, 16 09 2013. [Online]. Available: http://www.comsol.com/blogs/which-turbulence-model-should-choose-cfd-application/. [Accessed 31 03 2014].

[24] T. von Kármán, Mechanische Ähnlichkeit und Turbulenz, Proc. 3rd International Congress on Applied Mechanics Stockholm, 1930.

[25] J. H. Preston, "The Determination of Turbulent Skin Friction by means of Pitot Tubes.," J. Roy. Aero. Soc. 58, 109, 1954.

[26] J. Nikuradse, "Law of flow in rough pipes," N.A.C.A Tech. Mem. 1292 (Translation), 1950.

[27] L. Prandtl, "Zur turbulenten Strömung in Rohren und längs Platten," Ergebnisse der Aerodynamischen Versuchsanstalt zu Göttingen, Part IV, München, 1932.

[28] H. Schlichting, "Lecture series 'Boundary layer theory' Part I - Laminar flows," N.A.C.A. T.M. 1217, 1949.

[29] M. Bernardini, S. Pirozzoli and P. Orlandi, "Velocity Statistics in Turbulent Channel Flow up to Re_τ=4000," J. Fluid Mech. vol 742, 2013.

[30] P. S. Klebanoff, "Characteristics of Turbulence in a Boundary Layer with Zero Pressure Gradient," N.A.C.A. tech. Note 3178, 1954.

[31] D. Coles, "The Law of the Wake in the Turbulent Boundary Layer," J. Fluid Mech., Vol 1, 1956.

[32] T. Cebeci and A. M. O. Smith, Analysis of Turbulent Boundary Layers, Academic Press, 1974.

[33] F. H. Clauser, "Turbulent Boundary Layers in Adverse Pressure

Gradients," Journal of the Aeronatical Science, Vol. 21, 1954.

[34] P. R. Spalart and J. H. Watmuff, "Experimental and Numerical Study of Turbulent Boundary Layer with Pressure Gradient," J. Fluid Mech., Vol. 249, 1993.

[35] Y. Nagano, M. Tagawa and T. Tsuji, "Effects of Adverse Pressure Gradients on Mean Flows and Turbulence Statistics in a Boundary Layer," Eight Symp. on Turbulent Shear Flows, Springer, 1992.

[36] Z. Harun, "The Structure of Adverse and Favourable Pressure Gradient in Turbulent Boundary layers, PhD. Thesis," University of Melbourne, 2012.

[37] P. E. Skåre and P. Krogstad, "A Turbulent Equilibrium Boundary Layer near Separation," J. Fluid Mech., Vol. 272, 1994.

[38] V. C. Patel and M. R. Head, "Reversion of Turbulent to Laminar Flow," J. Fluid Mech., Vol. 34, 1968.

[39] R. F. Blackwelder and S. G. Kovasznay, "Large-Scale Motion of a Turbulent Boundary Layer during Relaminarization," J. Fluid Mech., Vol. 53, 1972.

[40] M. A. Badri Narayanan and V. Ramjee, "On the Criteria for Reverse Transition in a Two-Dimensional Boundary Layer Flow," J. Fluid Mech., Vol. 35, 1969.

[41] B. E. Launder, "Laminarization of the Turbulent Boundary Layer by Acceleration," MIT Gas Turbine Lab. Rep. 77, 1964.

[42] B. S. Baldwin and T. J. Barth, "A one-equation Turbulence Transport Model for High Reynolds number Wall-Bounded Flows," NASA TM - 102847, 1990.

[43] C. L. Rumsey and P. R. Spalart, "Turbulence Model Behaviour on Low Reynolds number Regions of Aerodynamic Flow Fields," AIAA Fluid Dynamics Conference and Exhibit, 2008.

[44] P. R. Spalart and S. R. Allmaras, “A One-Equtaion Turbulence Model for Aerodynamic Flows,” American Institute of Aeronautics and Astronautics, AIAA-92-0439, 1992.

[45] W. P. Jones and B. E. Launder, “The Prediction of Laminarization with a Two-Equation Model of Turbulence,” J. Heat Mass Transfer, 1972.

[46] V. Patel, W. Rodi and G. Scheuerer, “Turbulence Models for Near-Wall and Low Reynolds Number Flows: A review,” AIAA Journal, 1984.

[47] F. R. Menter, “Two-Equation Eddy-Viscosity Turbulence Models for Engineering Applications,” AIAA J. 32, 1994.

[48] H. K. Versteeg and W. Malalasekera, An introduction to Computational Fluid Dynamics - The Finite Volume Method, Longman Scientific & Technical, 1995.

[49] J. H. Ferzinger and M. Peric, Computational Methods for Fluid Dynamics, Springer, 2002.

[50] C. Habchi, S. Russeil, D. Bougeard, J.-L. Harion, T. Lemenand, A. Ghanem, D. Della Valle and H. Peerhossaini, “Partitioned Solver for Strongly Coupled Fluid-Structure Interaction,” Computers & Fluids, 2012.

[51] S. V. Patankar and D. B. Spalding, “A Calculation Precedure for Heat, Mass and Momentum Transfer in Three-Dimensional Parabolic Flows,” J. Heat Mass Transfer, 1971.

[52] R. I. Issa, “Solution of the Implicit Discretised Fluid Flow Equations by Operator-Splitting,” Journal of Computational Physics, 1985.

[53] H. Jasak, “Error Analysis and Estimation for the Finite Volume Method with Applications to Fluid Flows,” Imperial College of Sience, London, 1996.

[54] T. Behrens, “OpenFOAM's Basic Solvers for Linear Systems of Equations,” Chalmers, Department of Applied Mechanics, 18 02 2009. [Online]. Available:

http://www.tfd.chalmers.se/~hani/kurser/OS_CFD_2008/TimBehrens/tibeh-report-fin.pdf. [Accessed 26 06 2014].

[55] E. Caraba, "Preconditioned Conjugate Gradient Algorithm," 03 2008. [Online]. Available: http://ews.uiuc.edu/~caraba1/Projects/Thesis.pdf. [Accessed 27 06 2014].

[56] D. Katritsis, L. Kaiktsis, A. Chaniotis, J. Pantos, E. Efstathopoulos and V. Marmarelis, "Wall Shear Stress: Theoretical Considerations and Methods of Measurement," Progress in Cardiovascular Diseases, Vol. 49, 2007.

[57] Nabla Ltd., "4.5 Solution and Algorithm Control," Nabla Ltd., 2000-2007. [Online]. Available: http://www.foamcfd.org/Nabla/guides/UserGuidese15.html. [Accessed 26 06 2014].

[58] K. R. Sreenivasan, "The Turbulent Boundary Layer," Frontiers in Experimental Fluid Mechanics, 1989.

[59] S. Monte, P. Sagaut and T. Gomez, "Analysis of Turbulent Skin Friction Generated in Flow Along a Cylinder," Phys. Fluids, 2011.

[60] R. H. Nichols, "Turbulence Models and their Application to Complex Flows, Revision 4.01," [Online]. Available: http://people.nas.nasa.gov/~pulliam/Turbulence/Turbulence_Guide_v4.01.pdf. [Accessed 30 06 2014].

[61] S. R. Allmaras, F. T. Johnson and P. R. Spalart, "Modifications and Clarifications for the Implementation of the Spalart-Allmaras Turbulence Model," ICCFD7, 2012.

[62] P. R. N. Childs, Rotating Flow, Elsevier, 2011.

A OpenFOAM control files

A.1 controlDict

```
/*--------------------------------*- C++ -*----------------------------------*\
| =========                 |                                                 |
| \\      /  F ield         | OpenFOAM: The Open Source CFD Toolbox           |
|  \\    /   O peration     | Version:  2.2.2                                 |
|   \\  /    A nd           | Web:      www.OpenFOAM.org                      |
|    \\/     M anipulation  |                                                 |
\*---------------------------------------------------------------------------*/
FoamFile
{
    version     2.0;
    format      ascii;
    class       dictionary;
    location    "system";
    object      controlDict;
}
// * * * * * * * * * * * * * * * * * * * * * * * * * * * * * * * * * * * * //

application     pimpleFoam;

startFrom       startTime;

startTime       0;

stopAt          endTime;

endTime         60;

deltaT          0.001;

writeControl    runTime;

writeInterval   20;

purgeWrite      0;

writeFormat     ascii;

writePrecision  8;

writeCompression off;

timeFormat      general;

timePrecision   8;

runTimeModifiable false;


functions
{

       forces
        {
```

```
            type                forces;
            functionObjectLibs  ("libforces.so");
            outputControl       timeStep;
            outputInterval      1;
            patches             ( cylinder );
            pName               p;
            UName               U;
            rhoName             rhoInf;
            rhoInf              1000;
            log                 true;
            CofR                (0 0 0);
        }

        forceCoeffs
        {
            type                forceCoeffs;
            functionObjectLibs  ("libforces.so");
            outputControl       timeStep;
            outputInterval      1;
            patches             ( cylinder );
            pName               p;
            UName               U;
            rhoName             rhoInf;
            rhoInf              1000;
            magUInf             10.7;
            log                 true;
            liftDir             (0 1 0); //Acts perpendicular to flow
                                         //direction.
            dragDir             (1 0 0); //Acts in the flow direction.
            CofR                (0 0 0);
            pitchAxis           (0 1 0);
            lRef                0.1818; //Diameter of cylinder.
            Aref                0.033;  //Projected area in yz-plane.
                                        //Aref=lRef*height=0.1818*0.1818
        }

}

// ************************************************************************* //
```

A.2 fvSchemes

```
/*--------------------------------*- C++ -*----------------------------------*\
| =========                 |                                                 |
| \\      /  F ield         | OpenFOAM: The Open Source CFD Toolbox           |
|  \\    /   O peration     | Version:  2.2.2                                 |
|   \\  /    A nd           | Web:      www.OpenFOAM.org                      |
|    \\/     M anipulation  |                                                 |
\*---------------------------------------------------------------------------*/
FoamFile
{
    version     2.0;
    format      ascii;
    class       dictionary;
    location    "system";
    object      fvSchemes;
}
// * * * * * * * * * * * * * * * * * * * * * * * * * * * * * * * * * * * * * //

ddtSchemes
```

```
{
    default              CrankNicolson 0.95;
}

gradSchemes
{
    default                       Gauss linear;
    grad(p)                       Gauss linear;
    grad(U)                       Gauss linear;
}

divSchemes
{
    default                      none;
    div(phi,U)                   Gauss linear;
    div(phi,nuTilda)             Gauss linear;
    div((nuEff*dev(T(grad(U))))) Gauss linear;
}

laplacianSchemes
{
    default                              none;
    laplacian(nu,U)               Gauss linear corrected;
    laplacian(nuEff,U)            Gauss linear corrected;
    laplacian(rAUf,p)             Gauss linear corrected;
    laplacian((1|A(U)),p)                Gauss linear corrected;
    laplacian(DnuTildaEff,nuTilda) Gauss linear corrected;
}

interpolationSchemes
{
    default                      linear;
    interpolate(HbyA)    linear;
    interpolate(U)               linear;
}

snGradSchemes
{
    default         orthogonal;
}

fluxRequired
{
    default         no;
    p               ;
}
// ************************************************************************* //
```

A.3 fvSolution

```
/*--------------------------------*- C++ -*----------------------------------*\
| =========                 |                                                 |
| \\      /  F ield         | OpenFOAM: The Open Source CFD Toolbox           |
|  \\    /   O peration     | Version:  2.2.2                                 |
|   \\  /    A nd           | Web:      www.OpenFOAM.org                      |
|    \\/     M anipulation  |                                                 |
\*---------------------------------------------------------------------------*/
FoamFile
{
    version     2.0;
    format      ascii;
    class       dictionary;
    location    "system";
    object      fvSolution;
}
// * * * * * * * * * * * * * * * * * * * * * * * * * * * * * * * * * * * * * //

solvers
{
    p
    {
        solver          PCG;
        preconditioner  DIC;
        tolerance       1e-07;
        relTol          0.05;
    }

    pFinal
    {
        solver          PCG;
        preconditioner  DIC;
        tolerance       1e-07;
        relTol          0;
    }

    "(U|nuTilda)"
    {
        solver          PBiCG;
        preconditioner  DILU;
        tolerance       1e-06;
        relTol          0.05;
    }

    "(U|nuTilda)Final"
    {
        $U;
        tolerance       1e-06;
        relTol          0;
    }
}

PIMPLE
{
    nOuterCorrectors 1;
    nCorrectors     2;
    nNonOrthogonalCorrectors 1;
    pRefCell        0;
    pRefValue       0;
}

// ************************************************************************* //
```

A.4 fvOptions

```
/*--------------------------------*- C++ -*----------------------------------*\
| =========                 |                                                 |
| \\      /  F ield         | OpenFOAM: The Open Source CFD Toolbox           |
|  \\    /   O peration     | Version:  2.2.2                                 |
|   \\  /    A nd           | Web:      www.OpenFOAM.org                      |
|    \\/     M anipulation  |                                                 |
\*---------------------------------------------------------------------------*/
FoamFile
{
    version     2.0;
    format      ascii;
    class       dictionary;
    location    "system";
    object      fvOptions;
}
// * * * * * * * * * * * * * * * * * * * * * * * * * * * * * * * * * * * * * //


momentumSource
{
    type            pressureGradientExplicitSource;
    active          on;            //on/off switch
    selectionMode   all;       //cellSet // points //cellZone

    pressureGradientExplicitSourceCoeffs
    {
        fieldNames  (U);
        Ubar        (10.7 0 0);
        gradP0    gradP0 [0 1 -2 0 0] 1e-02;    // initial pressure-gradient
        flowDir     (1 0 0);                    // flow direction
    }
}

// ************************************************************************* //
```